UNIVERSITEIT VAN AMSTERDAM

VU VRIJE UNIVERSITEIT AMSTERDAM

MSc Physics
Science for Energy and Sustainability
Master Thesis

Decoupling Processes in Tandem Solar Subcells under Standard Operating Conditions by Combining Modulated Techniques

Author:	Maximilian K. H. Mundt
First Examiner:	Prof. Dr. Bruno Ehrler
Second Examiner:	Prof. Dr. Erik Garnett
Daily Supervisor:	Dr. Agustin Alvarez

July 8th, 2025

AMOLF physics of functional complex matter

Abstract

With the ever-increasing impact of the Global North on the environment and the Global South, large-scale changes are needed to make our practices sustainable again. Among these necessary adaptations is the large-scale deployment of renewable energy-generation technologies worldwide. As electricity demands are projected to increase drastically over the next decades, solar technologies are being optimized to increase their energy yield.

Among these technologies are tandem solar cells, which utilize multiple absorber layers to increase their theoretical efficiency. However, depending on the device architecture, optimal operation requires multiple processes to occur simultaneously, leading to complex interactions between them. As this technology presents a useful tool for advancing the energy transition, it is crucial to gain more understanding of the physics governing its behavior to more effectively improve its power-conversion efficiency.

Thus, in this master's thesis, a novel method for characterizing tandem solar cell processes under solar operating conditions is presented. Utilizing light-modulation techniques via independent light-emitting diodes, the subcells are distinguished from one another without light flooding, which is shown to impact subcell behavior. Furthermore, individual recombination and transport processes within subcells are quantified, allowing for a detailed analysis of which behaviors are affected by internal or external conditions. Finally, by repeating measurements under different strengths of sun-equivalent illuminations, subcell behaviors over different voltages can be determined, leading to further knowledge on subcell current-voltage responses. Thereby, this method will hopefully contribute to sustainable development by providing researchers with a tool to analyze individual tandem solar cell behaviors under real-world illumination conditions.

List of Abbreviations

2T	2-terminal
CPE	constant phase element
EC	equivalent circuit
EQE	external quantum efficiency
GaAs	gallium arsenide
IMPS	intensity-modulated photocurrent spectroscopy
IMVS	intensity-modulated photovoltage spectroscopy
InGaP	indium gallium phosphide
J_{SC}	short-circuit current
JV	current-voltage
LED	light-emitting diode
TSC	tandem solar cell
V_{OC}	open-circuit voltage

Table of Contents

1 Introduction

Solar cell production has grown exponentially due to the need for a clean energy transition [1]. Most of these solar cells are produced from stable silicon, which boasts a record of 27.6% efficiency in lab settings [2]. However, this record efficiency has only improved little over the last three decades, as these devices approach their theoretical detailed balance limit of 29.8% [3]. Since large-scale infrastructural, technological, and behavioral changes are still needed to meet climate goals [4], it is crucial that new strategies are developed to overcome these barriers.

Thus, research into tandem solar cells (TSCs) has gained increasing attention [5] as the addition of a second absorber layer greatly increases the theoretical limit for power conversion efficiency [6]. For this second layer, metal halide perovskite semiconductors are very attractive due to their tunable, direct bandgap, which allows perfect matching of absorption spectra as well as little material needed to produce an efficient absorber [7]. However, significant improvements are still needed, as is evident from the gap between the record efficiency of perovskite/silicon TSCs at 34.9% [2] and their detailed balance limit of 42.3% [6].

To continue driving improvements, it is useful to understand where the main problems in producing TSCs lie, such that research can be efficiently directed to where it is most needed. Performing current-voltage (JV) measurements is a quick and easy method to assess the performance of a device, though the information that can be extracted is limited, especially in 2-terminal (2T) devices [8].

Thus, methods have been developed to study the subcells individually [9]. Usually, these measurements involve using photons of a wavelength only absorbed by one subcell to saturate it with free electrons. This strategy makes the saturated subcell effectively invisible to electrical measurements, allowing the non-saturated subcell to be investigated individually, for example, in external quantum efficiency (EQE) and absorption measurements [10,11], capacitance-voltage experiments [12], and thermal admittance spectroscopy [13]. Furthermore, electroluminescence has been used to determine the current-voltage responses of individual subcells [14,15], whereas photoluminescence has helped in mapping the subcells' voltages under different illumination conditions [16].

Additionally, impedance spectroscopy has been used to disentangle the different processes in a device [17-20]. However, this technique produces data that can be interpreted in multiple ways, as seen in the different equivalent circuits (ECs) chosen by Zarazua et al. [21], Yoo et al. [22], and Seyed-Talebi and Kazeminezhad [23]. The multitude of interpretations of a given impedance spectrum also implies ambiguity in attributing observed impedance arcs to specific physical processes in a device [24].

To partially combat this latter issue, Roose et al. [25] have measured the impedance of a perovskite/perovskite TSC with two separate light-emitting diodes (LEDs) corresponding to each subcell's absorption spectrum. By using the technique of saturating one subcell at a time with one of the LEDs, they could thus measure the other subcell individually. When comparing the resulting spectra to the impedance of the TSC under current-matching conditions using the characteristic frequencies, the subcells could effectively be disentangled from one another. Similarly, Park et al. [26] used a perovskite/silicon device with 2T and 3-terminal contacting to show that flooding a subcell with light effectively makes it invisible for impedance.

However, even though the setups of Roose et al. [25] and Park et al. [26] offer these useful additional insights, the decision to light-flood one subcell comes at the expense of not being at standard operating conditions. This is especially limiting in perovskite subcells, where the mobile ion distribution, which is affected by illumination, can determine device functionality

[27,28]. Furthermore, the measurements face the same drawback of regular impedance experiments in that it is unclear whether an identified process is due to recombination or transport.

To mitigate this issue, Alvarez et al. [29] have recently used intensity-modulated photocurrent spectroscopy (IMPS) and intensity-modulated photovoltage spectroscopy (IMVS) on single-junction solar cells to supplement impedance measurements. Using the optical properties of their solar cells, this combination of techniques allows a deeper understanding of the origin of the different observed processes, clearly separating recombination and transport. Additionally, one can extract additional parameters, such as the efficiency at which photons are absorbed and energetically separated, as well as the differential external quantum efficiency (EQE_{diff}) of one's device at different voltages. As light-modulated techniques depend on the absorptive properties of the device being measured, they therefore present an interesting tool for a new characterization method of TSCs.

Thus, in this work, impedance spectroscopy, IMPS, and IMVS are used on TSCs to identify the impedance effects of each subcell by using two independent LEDs. The techniques are first explored on a silicon photodiode and a perovskite solar cell to observe and understand the relationships between the different techniques. Next, these methods are verified on a III-V TSC by comparing light-flooded and equal-illumination responses of the subcells. This step highlights the importance of characterizing subcells under solar operating conditions, as light-flooding alters the observed responses. Afterward, the techniques are applied to a perovskite/silicon TSC to analyze the behaviors of various processes and how they change as a result of degradation. Finally, using different sun-equivalent offset illuminations, the voltage-dependence of the observed behaviors is analyzed. Using these insights, JV responses of the individual subcells as they operate in the full TSC could be reconstructed by combining the trends in the observed parameters.

Thereby, due to the advantages of IMPS and IMVS, the same improvements to impedance spectroscopy on TSCs are demonstrated as the methods of Roose et al. [25] and Park et al. [26], while introducing new insights without the drawbacks of flooding a subcell. Aside from assigning a TSC's processes to its subcells, the extent to which a given impedance feature originates from recombination or transport could be quantified while remaining in sun-equivalent conditions. Thus, this method will, ideally, provide a useful tool to enhance TSC characterization and their improvements by providing insights into the mechanisms governing a device's performance and how changes in internal and external conditions may affect various behaviors.

2 Theoretical Background

2.1 Perovskite

With their rapidly increasing record power conversion efficiencies [2], perovskite solar cells are rapidly gaining popularity for applications in solar energy [30]. A large reason for this is their crystal structure (see Figure 1), which is easily synthesized [31] and provides a direct, tunable bandgap [7]. This means that the active layer can reach high efficiencies even for thicknesses of only a few nanometers, leading to high cost efficiency, low weight, and the possibility to create flexible films that can be bent to adapt to many different types of surfaces.

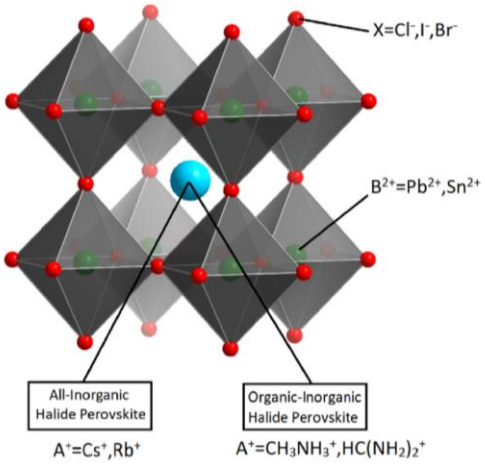

Figure 1. Perovskite crystal structure, as depicted by Dai et al. [32].

Despite these advantages, however, perovskite also has several drawbacks that hinder its market readiness as a solar-cell material [33]. Firstly, due to its ionic structure, its stability is greatly dampened by exposure to environmental influences such as oxygen or water [34]. Additionally, ion migration driven by electrical biasing and illumination can play a large role in degrading the device, which may change or even destroy the crystal structure, leading to significant performance decreases [35]. Though some strategies have been developed to mitigate these issues, they remain a significant roadblock to the commercialization of perovskite devices [36].

Nonetheless, due to its many beneficial properties that also allow it to be paired with other materials to form TSCs, perovskite is clearly set on the roadmap as a crucial material for the energy transition [37]. Therefore, it is vital to continue researching this material on its own and when integrated into devices to identify mechanisms that can combat its drawbacks.

2.2 2-Terminal Tandem Solar Cells

Unlike single-junction solar cells, TSCs possess multiple active layers whose electrons are excited by light of different energies (see Figure 2 and [6,38]). Based on the bandgap of an absorber's material, it will transform photons with energies above its bandgap energy into an electronic current while transmitting photons of lower energies. Thus, TSCs will have a high-bandgap material on the top to absorb high-energy photons with little thermalization losses, while the lower-energy light is transmitted and absorbed by a subsequent layer. To utilize the increase in energy of the free charges in 2T TSCs, a recombination layer between active layers facilitates the recombination of a hole from one absorber layer with an electron from the other layer [39]. Thus, there is a large energy gap between the extracted electron and hole, leading to a greatly increased voltage during charge extraction [38,39].

This mechanism, however, requires an equal number of free photogenerated charges in the two neighboring active layers [38,39]. If there is an excess number of charges in one subcell, there are no opportunities to recombine with a charge from the other subcell. Thus, due to charge conservation, the mobile carriers will have to recombine within the subcell since they cannot be extracted.

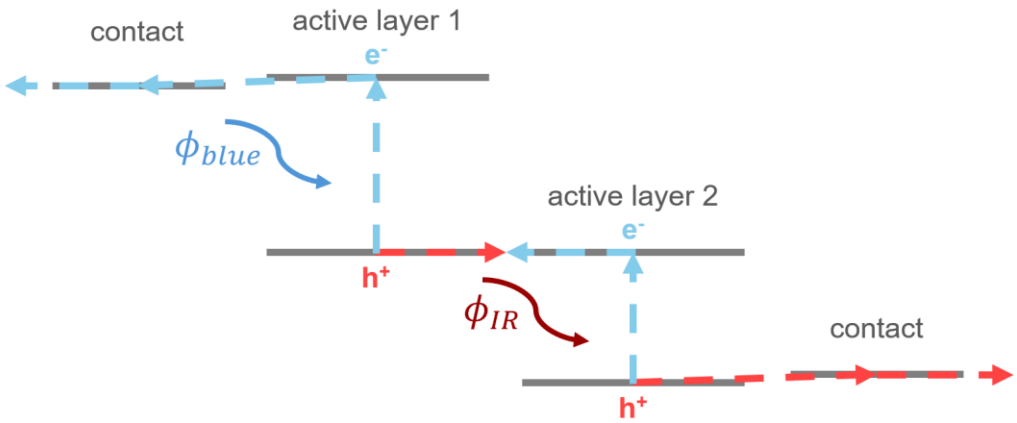

Figure 2. Simplified diagram of photogenerated charge extraction in a 2-terminal tandem solar cell. The higher-energy photons absorbed by the top subcell are exemplified by a blue photon, whereas the lower-energy ones are exemplified by an infrared one.

This effect means that under mismatched conditions, the subcell with fewer photogenerated charge carriers will limit charge extraction. As the charge-saturated subcell thus effectively becomes less visible to electrical measurements, as its photoresistivity is decreased [21], a popular method for characterizing TSC subcells is to light-flood one subcell and change the experimental conditions for the other one. As the saturated subcell will not impact the electrical measurements, changes in signal are assumed to stem from the limiting subcell [10]. However, complications can arise when operating away from standard solar test conditions, such as parasitic absorption [11] and luminescence coupling [40], leading to responses influenced by the abundance of charges in the inactive absorber layer.

2.3 Impedance Spectroscopy

Impedance spectroscopy leverages the different characteristic times τ_0 of various processes that occur inside an electronic device [41]. By modulating the voltage around a fixed offset voltage $\bar{V}_{app}$, the current modulation response of a device $\tilde{J}_{inj}$, including the phase shift δ between the two, is tracked. Thus, the impedance Z of a device effectively is a frequency-resolved differential resistance function, as it calculates the ratio between the applied voltage perturbation $\tilde{V}_{app}$ and the measured current response:

$$Z = \frac{\tilde{V}_{app}}{\tilde{J}_{inj}} = \frac{|\tilde{V}_{app}|}{|\tilde{J}_{inj}|} e^{i\delta} = Re(Z) + Im(Z) = Z' + Z'', \quad (Eq.1)$$

where e is Euler's number, while Re and Im denote the real and imaginary components of a number, respectively.

At high frequencies, some capacitive or inductive processes may not be able to follow the voltage changes, such that their contribution to the current response is not observed. Only when the perturbation frequency f decreases does it become more likely to change current extraction. For capacitive processes, this leads to an arc positive in Z' and $-Z''$ which peaks at the characteristic frequency f_0, when the phase delay between $\tilde{V}_{app}$ and $\tilde{J}_{inj}$ is the largest. This arc is caused by more charges becoming impeded as they increasingly respond to the voltage changes with decreasing frequency. The opposite is true for inductive processes, which create an arc negative in Z' and $-Z''$. Thus, Z will overall increase for lower frequencies for capacitive processes, and decrease for inductive ones, until a full response from the processes can be measured. Therefore, at very low frequencies, impedance will be equal to the differential resistance R_{diff} at the given voltage as described by

$$Z\left(f \to 0\ Hz, \bar{V}_{app}\right) = \frac{d\bar{V}_{app}}{d\bar{J}_{inj}} = R_{diff}. \quad (Eq.2)$$

To analyze impedance spectra, many researchers use ECs [20,41,42]. In circuitry, impedance can be modeled using a combination of resistances R, capacitances C, and inductances L. In the EC, the constant resistance offset at very high frequencies is given by a series resistance R_s. To simulate the phase delays observed in impedance spectra, each positive arc is composed of an R-C pair with the two elements parallel to one another. The product of the two is equal to τ_0 given by

$$R * C = \tau_0 = \frac{1}{\omega_0} = \frac{1}{2\pi f_0}. \quad (Eq.\ 3)$$

However, by intertwining R-C pairs in one another, different ECs can be generated that will produce different parameter values while simulating the same data set. Furthermore, this may also imply different physical mechanisms, as further explored in section 2.4. Therefore, one must be careful when assigning an EC to impedance spectra. Nonetheless, ECs provide a useful tool as they allow us to quantify how different processes contribute to the overall resistance – and thus current responses – of a device at various voltages.

2.4 Intensity-Modulated Photocurrent and Photovoltage Spectroscopy

IMPS and IMVS are a pair of techniques similar to impedance in that they also measure an alternating response to a small perturbation. However, instead of applying a voltage perturbation, a light perturbation $\tilde{\phi}_{app}$ is applied, which is measured beforehand by calibrations (see section 9.3 and Appendix A). For IMPS, the voltage is held constant, for example, at the steady-state open-circuit voltage (V_{OC}), and the current response of the device is measured. In IMVS, the voltage response is measured while keeping the current constant, for example, at 0 A. Thus, the IMPS transfer function Q is given by the quotient of extracted current modulation $\tilde{J}_{ext}$ – which is the additive inverse of $\tilde{J}_{inj}$ – and the applied light perturbation (see $Eq.4$), likening it to a frequency-resolved differential EQE measurement. Conversely, the IMVS transfer function W is given by the ratio between the voltage response and the light perturbation (see $Eq.5$):

$$Q = \frac{\tilde{J}_{ext}}{q\tilde{\phi}_{app}} = Q' + Q'', \qquad Q\left(f \to 0\ Hz, \bar{V}_{app}\right) = \frac{1}{q}\frac{d\bar{J}_{ext}}{d\bar{\phi}_{app}} = EQE_{diff}\left(\bar{V}_{app}\right), \quad (Eq.4)$$

$$W = \frac{\tilde{V}_{app}}{q\tilde{\phi}_{app}} = W' + W'', \quad (Eq.5)$$

where q is the elemental charge. It is important to note that the value of EQE_{diff} only describes how the device's photoconversion changes with frequency, not the full extent of current generation. Thus, when calculating the total extracted current, it does not suffice to multiply EQE_{diff} by the photocurrent, but the dark current from the diode must be added as well.

As W and Q both have $q\tilde{\phi}_{app}$ in their denominator, one can divide W by Q to obtain

$$\frac{W}{Q} = Z, \quad (Eq.6)$$

as shown by Alvarez et al. [29]. Thus, IMPS and IMVS lend themselves to be compared to impedance spectroscopy as the combination of two datasets can be used to calculate the third to confirm the uniformity of measurement conditions [29]. Due to these similarities to impedance, IMPS and IMVS can also be modeled using ECs, as seen from applications in minority charge carrier dynamics and voltage-dependent EQE measurements for IMPS [43] and minority charge carrier dynamics and charge-carrier lifetimes for IMVS [44]. Due to their dependence on photoexcitation, an additional element for a current source is added to the EC to indicate the conversion from light to current in the device. As no (alternating) current is

extracted from IMVS, all photogenerated current must be recombined, meaning that any elements parallel to this current must be related to recombination [29].

The conversion from light to free charge carriers depends on the photon being absorbed and generating an energetically separated electron-hole pair. Therefore, Q and W are proportional to the so-called absorption-separation efficiency η_{as} [29]. Thus, by dividing $Q(f \to 0\,Hz)$ by η_{as}, one can calculate the extraction efficiency η_{ext} of the charge carriers. Similarly, dividing η_{as} by the photon-absorption efficiency η_{abs} of the device, determined, for example, using reflection measurements, one can find the efficiency η_{sep} at which electron-hole pairs are energetically separated. Thus, the different aspects forming a device's EQE can be quantified using IMPS.

To simplify the fitting of Q and W data with ECs, the different elements can be categorized depending on where they are located relative to the injected photocurrent (see Figure 3 (left) and Alvarez et al. [29]). Recombination processes, which are dependent on photoabsorption, are named recombination impedance Z_{rec}. For capacitive processes, they are thus comprised of the recombination resistance R_{rec} and a capacitor C_{rec} that is parallel only to R_{rec}. If there are multiple processes dependent on photoabsorption, all elements parallel to the generated photocurrent are included in Z_{rec}. Therefore, all recombination resistors become elements of Z_{rec} (see Figure 3 (right)). Processes parallel to Z_{rec} can be grouped as parallel impedances Z_p. Processes that follow Z_{rec} in series and share a parallel element with it are denoted as Z_f. Lastly, elements completely separated from Z_{rec} can be classified as series impedances Z_s. Thus, we use the equations formulated by Alvarez et al. [29] for Q and W:

$$Q = \frac{\eta_{as}}{Z_s}\frac{Z_{rec}}{Z_{rec}+Z_f}\left(\frac{1}{Z_s}+\frac{1}{Z_p}+\frac{1}{Z_{rec}+Z_f}\right)^{-1}, \quad (Eq.7)$$

$$W = \eta_{as}\frac{Z_{rec}}{Z_{rec}+Z_f}\left(\frac{1}{Z_p}+\frac{1}{Z_{rec}+Z_f}\right)^{-1}. \quad (Eq.8)$$

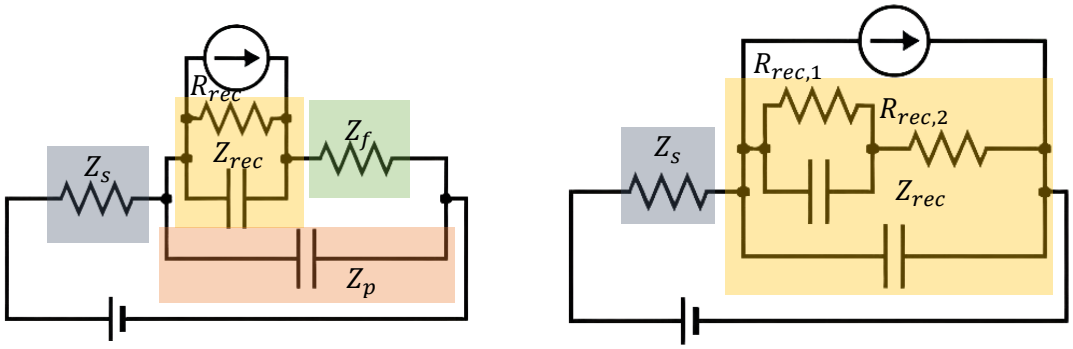

Figure 3. Visualization of equivalent circuit elements for calculating Q and W. Z and R denote impedance and resistance, respectively. The subscripts "s", "rec", "f", and "p" stand for "series", "recombination", "following", and "parallel", respectively.

From the equation for Q, we can thus also find η_{ext} as a frequency-dependent function of the different impedance elements. The DC value for η_{ext} can be found simply by using the different values for the EC resistances.

From visually analyzing these photocurrent-driven ECs, we see how IMPS and IMVS are able to distinguish between recombination and transport elements. Unlike in impedance, where Z_f and Z_p are parallel to each other, the absorption-induced current will cause Z_p to effectively be in series to Z_f while being parallel to Z_s for $\tilde{J}_{ext}$. Thus, a transport resistance R_{tra}, which could be placed at Z_f coupled with a capacitance as Z_p (see Figure 3 (left) and [29]),

would lead to a very different result in IMPS and IMVS than a second recombination resistance R_{rec} (see Figure 3 (right)), as it would become a competing process to the (first) recombination resistance rather than simply being in series.

This distinction of the EC elements also reveals how recombination and transport have contrasting roles when modeling a photovoltaic device. Since IMPS measures the extent to which charges are extracted from an active layer, the elements should be such that the current response is maximized for any given voltage. Therefore, elements that are not the recombination resistance, i.e. transport resistances, should be small such that current can flow easily out of the absorber to be extracted. In contrast, the recombination resistance itself should be high such that the generated current does not remain in the active layer and simply recombine. When measuring at voltages higher than the voltage of maximum power (V_{MPP}), though, the recombination resistances may decrease as more charges are extracted. Thus, depending on $\bar{V}_{app}$, the fill factor, and V_{MPP}, it may even be desirable to have a lower recombination resistance, since a high fill factor will lead to a high current-voltage slope for $\bar{V}_{app} > V_{MPP}$.

IMVS, on the other hand, is a useful tool to investigate the processes of only the perturbed layer. Since no current is extracted, all the current generated by the photoconversion must recombine within the device itself, unless there is a shunt resistance coupling the perturbed layer with another layer (see Appendix B). Therefore, only elements linked to Z_{rec} that are not a part of Z_s will provide a response during IMVS.

Therefore, the combination of these light-modulation techniques provides powerful insights that surpass those provided by impedance spectroscopy or light-flooding alone. By illuminating the subcells equally while modulating only one light, we can observe the optical and impedance properties, the individual subcell processes through IMVS, and the interaction between an individual subcell and the rest of the TSC.

3 Preliminary Studies on Small-Perturbation Techniques

To gain a first intuition for small-perturbation techniques, we perform measurements on single-junction solar cells. By recreating the study by Alvarez et al. [29] on a silicon photodiode, we can see how impedance, IMPS, and IMVS impact each other using simulations via ECs. The knowledge gained from how the placement of photogeneration in an EC impacts spectra derived from IMPS and IMVS is then used to identify processes in a perovskite solar cell that are not apparent from only looking at the impedance spectrum.

3.1 Results

3.1.1 Silicon Photodiode

The interaction of the impedance, IMPS, and IMVS transfer functions (in silicon photodiodes) has already been extensively studied by Alvarez et al. [29]. As this interplay has a key role in our proposed method for understanding subcell processes in TSCs, we begin by recreating a well-understood system. In contrast to Alvarez et al., though, we focus here less on identifying which processes in the photodiode are due to recombination and charge transport but rather on how different interpretations of a given impedance spectrum will impact predicted results for Q and W.

Measuring the impedance spectrum for our photodiode reveals similar features as Alvarez et al. [29] (see Figure 4a): We observe a smaller feature at high frequencies and a larger one for somewhat lower frequencies. Although the high-frequency feature has been identified as a diffusion-related process, it is common to model it as an R-C pair [29]. We observe that although several interpretations are valid (see ECs in Figure 4b), all lead to the

same impedance spectrum. Thus, it is unclear whether a given impedance arc is caused by recombination or transport resistance.

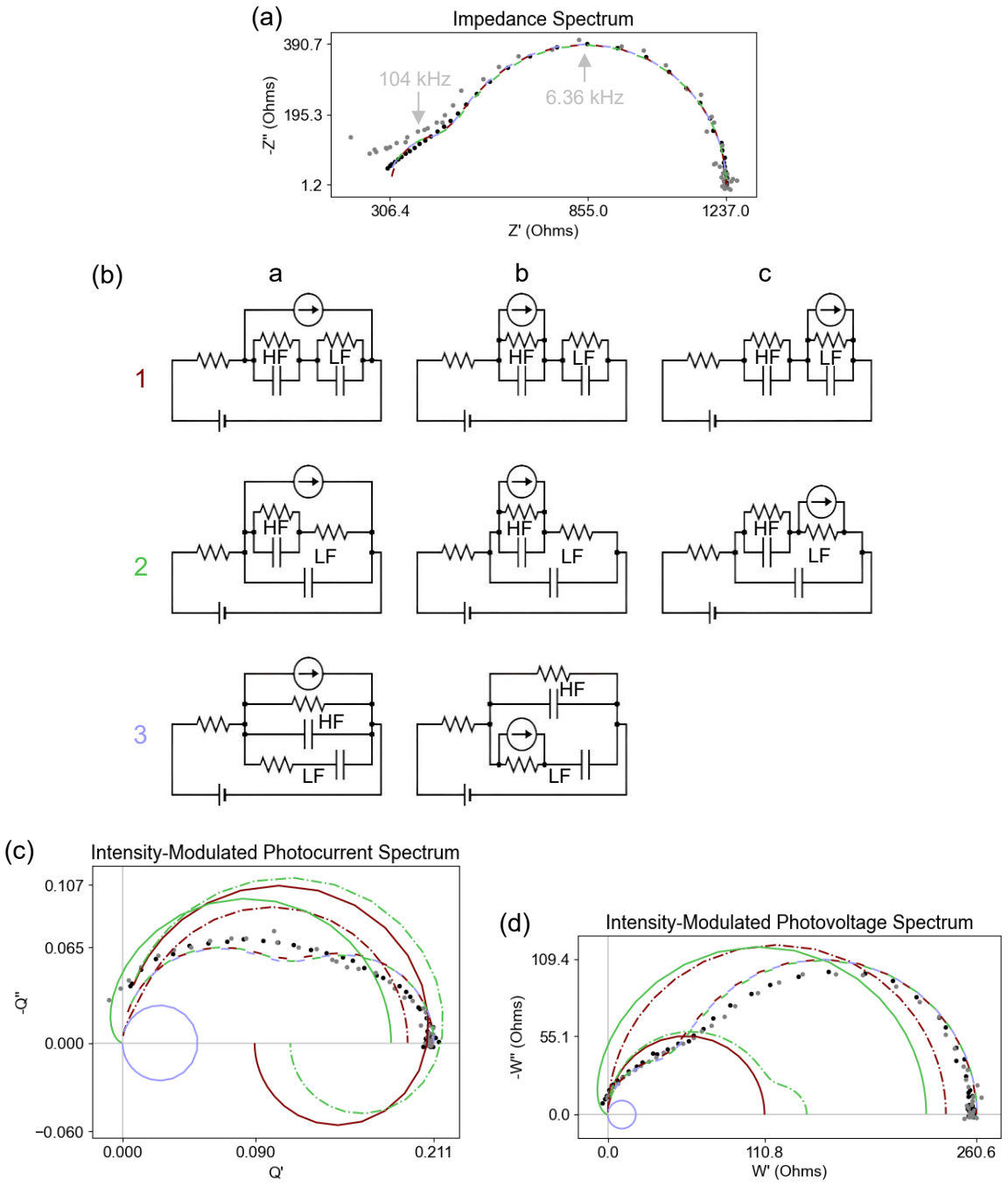

Figure 4. (a) Impedance spectrum of a silicon photodiode at open-circuit voltage compared to the quotient of the measured IMVS and IMPS data, and curve fits for the three possible equivalent circuit types. The black dots represent the measured data for Z, whereas the gray dots are the impedance recreated from the IMPS and IMVS measurements; The colors dark red, green, and light blue represent, respectively (b) the equivalent circuits used for fitting the data; the numbers refer to the three possible circuits, each having multiple photogeneration options – which are neglected in the curve fits due to their lack of impact on the impedance – with the variants differentiated by the letters above the columns. The abbreviations HF and LF refer to the resistance-capacitance pairs being attributed to the high-frequency and low-frequency features, respectively. (c) Intensity-modulated photocurrent spectrum and (d) intensity-modulated photovoltage spectrum at open-circuit voltage compared to simulations based on the data from the impedance spectrum. The dashed, solid, and dot-dashed line types correspond to the a, b, and c variants of the equivalent circuits, respectively. The device was measured over a frequency range of 1 MHz - 10 Hz at open-circuit voltage while illuminated at an equivalent of 0.02 suns.

Therefore, to determine the origin of the impedance features, the various EC options are used to simulate results for Q and W and compared to the measured IMPS and IMVS data (see Figures 4c and d). It is clear that only the interpretations that identify both impedance elements as recombination processes lead to a coherent picture (parameter values for EC 2a are found in Appendix C), as these ECs are the only ones leading to two arcs in both Q and W as well. We can also note that the arcs approximately share characteristic frequencies between the three data sets. Furthermore, we observe that only EC 2b leads to data points in the second quadrant. As the second R-C pair in EC 2b is in series and parallel to the recombination process, IMPS and IMVS data that take this shape can be interpreted as a photoconversion process whose extraction faces internal resistance due to transport by this enveloping R-C.

3.1.2 Perovskite Solar Cell

Using the knowledge gained from section 3.1.1, we investigate the impedance data of a perovskite solar cell. In all three spectra, we note two positive arcs (see Figure 5); From the impedance spectrum, we infer that we have two dominant R-C processes, whereas from IMPS and IMVS, we conclude that both of these processes are recombination, as the data corresponds to graphs for the a-type ECs (see Figure 4). Based on past studies, we can thus conclude that the high-frequency arc is caused by electronic recombination, whereas the low-frequency arc is caused by ions [42]. Thus, we model our system as seen in Figure 5, with the parallel resistance and capacitance elements describing the high-frequency arc, and the low-frequency arc described by the R-C pair lined up in series. Simulations of the IMPS and IMVS data for all possible ECs with 2 R-C pairs using the impedance spectrum can be found in Appendix D.

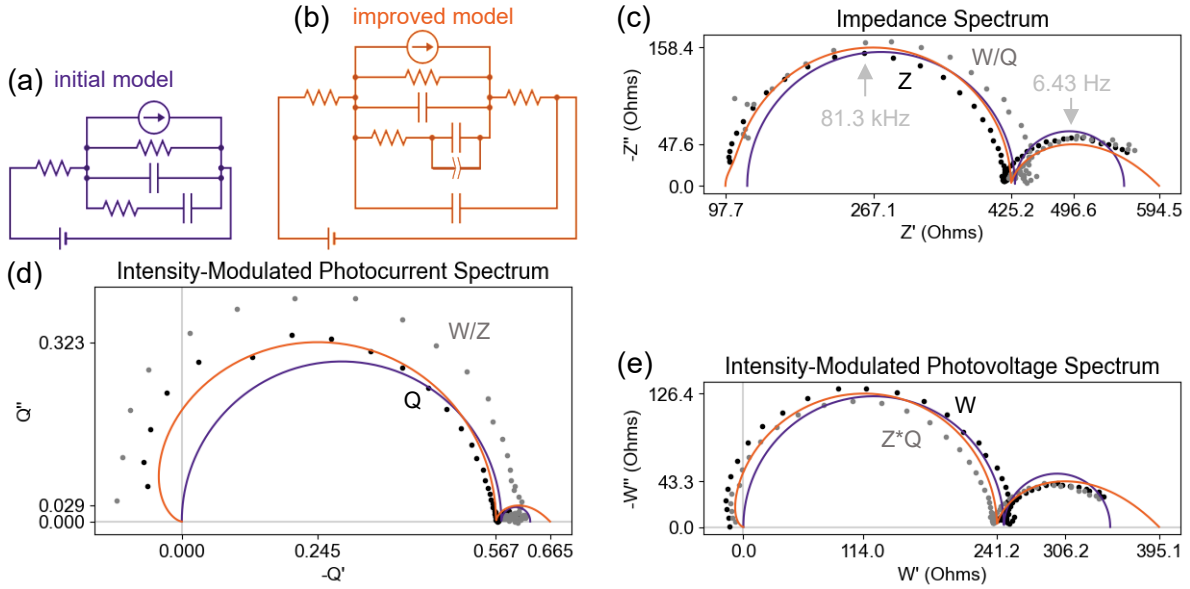

Figure 5. (a) Initial and (b) improved equivalent circuit to model (c) impedance, (d) IMPS, and (e) IMVS data of a perovskite solar cell at open-circuit voltage. The lines correspond to the fits in the colors of the equivalent circuits, whereas the measured data and reconstructed data using the other two techniques are displayed as black and gray dots, respectively. The device was measured over a frequency range of 1 MHz - 316 mHz at open-circuit voltage while illuminated at an equivalent of 0.1 suns.

However, when using only two R-C pairs to model our data, we notice that our system is only moderately well-described: The features in the second quadrant of Q and W are not captured in the model. Seeing how this feature arises when simulating Q and W for EC 2b (see Figures 4c and d), we can deduce that a transport R-C pair around the recombination elements is needed in the model to more accurately describe our system (see Figure 5). This feature would not be identifiable using the impedance spectrum alone and allows for a clear distinction between the contributions of recombination and transport to the overall impedance of the device (see Table 1). It also leads to a more accurate determination of R_s, as the addition of

the transport R-C pair allows for a more accurate, frequency-resolved impedance at high frequencies, as also evident by τ_{tra}.

Additionally, the low-frequency arc ends sooner in the model predictions than in the measurements. Therefore, in the improved model, we also add a constant phase element (CPE) parallel to the ionic capacitance to capture the effect of ionic diffusion implied by the widening of the arc [20,41] (see Figure 5). This added element also leads to a more accurate determination of $R_{rec,ion}$ (see Table 1), as the value decreases due to the widening of its arc. Furthermore, including CPE in the EC also has an important role in evaluating the optical characteristics of our device by describing η_{ext} more accurately (see Table 1). Thus, instead of underestimating EQE_{diff} as 72%, we find a more accurate value of 76%, a relative increase of over 5.5%.

Table 1. Extracted parameter values based on the initial model (left) and the improved model (right). The characteristic times τ are found following Bisquert and Balaguera [45]. The subscript "s" denotes series. The subscript "rec" denotes recombination, with the following abbreviations "ele" and "ion" describing the nature of the recombination to be electronic and ionic, respectively. The subscript "tra" denotes transport. The errors are the standard deviations from the curve fits after being rounded up, with those for τ, EQE_{diff}, and η_{ext} found via error propagation, using $Eq.3$ for the former, and the equation for Q ($Eq.7$) with DC values for the latter two. The values for the absorption efficiency are based on reflection measurements by the University of Potsdam [46] and the LED emission spectrum (see Appendix E). To find corrected values for EQE_{diff} and η_{ext} without the influence of the measurement equipment, the system is simulated without the instrument's internal resistance (see Appendix F).

Parameter (units)	Initial Model	Improved Model
R_s (Ω)	123 ± 3	99 ± 3
R_s, corrected (Ω)	51 ± 3	26 ± 3
$R_{rec,ele}$ (Ω)	432 ± 4	435 ± 6
$C_{rec,ele}$ (nF)	8.9 ± 0.3	4.5 ± 0.8
$\tau_{rec,ele}$ (μs)	3.8 ± 0.2	2.0 ± 0.4
$R_{rec,ion}$ $(k\Omega)$	1.06 ± 0.02	0.68 ± 0.02
$C_{rec,ion}$ (μF)	53 ± 3	36 ± 3
CPE_{Pvk} $(\mu F * s^{-0.5})$	N/A	24 ± 2
$\tau_{rec,ion}$ $(\mathrm{m}s)$	56 ± 4	25 ± 3
R_{tra} (Ω)	N/A	62 ± 4
C_{tra} (nF)	N/A	4.9 ± 0.7
τ_{tra} (μs)	N/A	0.30 ± 0.05
EQE_{diff} (%)	63 ± 2	67 ± 2
EQE_{diff}, corrected (%)	72 ± 2	76 ± 2
η_{abs} (%)	95.7	95.7
η_{sep} (%)	84.4 ± 0.7	95.0 ± 1.0
η_{ext} (%)	78 ± 2	73 ± 2
η_{ext}, corrected (%)	90 ± 2	83 ± 2

3.2 Intermediate Conclusions

In this section, we have used two devices, each using one of the active materials in the perovskite/silicon TSC used in section 5. From the silicon photodiode, we observed how various combinations of resistive elements lead to different IMPS and IMVS data shapes despite sharing an impedance spectrum. This revealed specifically that recombination elements lead to positive arcs in Z, Q, and W, whereas transport R-C pairs lead to a negative feature in Q' and W'.

From the perovskite solar cell, we observed that important parameters that may be hidden in the impedance spectrum can become apparent in data collected from IMPS and IMVS. Thus, a more detailed analysis can be performed, revealing how recombination and transport interact, and how ionic diffusion impacts charge extraction.

4 Small-Perturbation Measurements on a III-V Tandem Solar Cell

To investigate the advantage of using IMPS and IMVS for measuring TSCs, we make use of the optical properties of the two subcells. As perovskite is an unstable material due to mechanisms such as ion migration [35], we first show the strength of these methods on a stable system. Thus, we compare results from light-flooding vs. equal illumination on a III-V TSC, where the top subcell is made of indium gallium phosphide (InGaP) and the bottom subcell is made of gallium arsenide (GaAs). The parameter values resulting from the curve fitting of the TSC's small-perturbation data can be found in Appendix G.

Before investigating the processes of the subcells, we note a large negative feature at very high frequencies in the impedance spectrum that does not appear in the IMVS data of either subcell (see Figures 6b, d, and f). Since the device displays a high shunt resistance, as evidenced by the shallow slope at J_{SC} in the JV curve (see Appendix H), only the perturbed layer can contribute to the IMVS response since the photogenerated current can only remain within the perturbed subcell. As the feature persists under all three illumination conditions but in neither IMVS graph, it is likely that this feature is simply caused by the contacts.

Next, we analyze the top subcell. Based on the graph shapes in all three spectra, in which we observe a positive arc, this layer is governed by a recombination R-C pair. In the impedance spectrum, we observe the arc shrinking somewhat when light-flooding the GaAs subcell, implying that the arc is partially caused by the bottom subcell but also by the top one. When measuring IMPS and IMVS when perturbing the top subcell at the different illumination conditions, little change is observed due to the increased illumination of the bottom subcell. Especially from the IMVS, it becomes clear that the top GaInP itself is not affected by the increased far-red photon flux. Thus, both light-flooding and equal illumination are shown to be valid for measuring impedance and optical data in this subcell.

The same statement, however, does not apply to the bottom subcell; The IMVS response of this subcell is greatly affected by the increased blue-light intensity. Since the applied perturbation itself is unchanged, this means that the change in the top subcell's illumination is affecting the offset conditions at which the bottom subcell is measured. This observation can also be made from the impedance spectra resulting from the different illumination conditions, as the decrease in the impedance arc when light-flooding the top subcell is far larger than the resistance previously ascribed to the InGaP layer. This fact is further supported by the JV curves of the three illumination conditions, revealing a larger J_{SC} and, thus, V_{OC} as a result of flooding the top subcell (see Appendix H). Consequently, we can deduce that the operating point of the measurements has changed due to the increased illumination of the top cell.

A likely explanation for this phenomenon is luminescent coupling (depicted in Figure 7). As the top subcell has a very large photoluminescence quantum yield [14], it is likely that non-extracted electrons recombine radiatively. Since the bandgap of the InGaP subcell is 1.89 eV [47], these reemitted photons can be absorbed by the GaAs, leading to an artificially stronger excitation of the bottom subcell. This phenomenon has been recorded in JV measurements as well, where corrections are needed to account for this luminescent coupling [40].

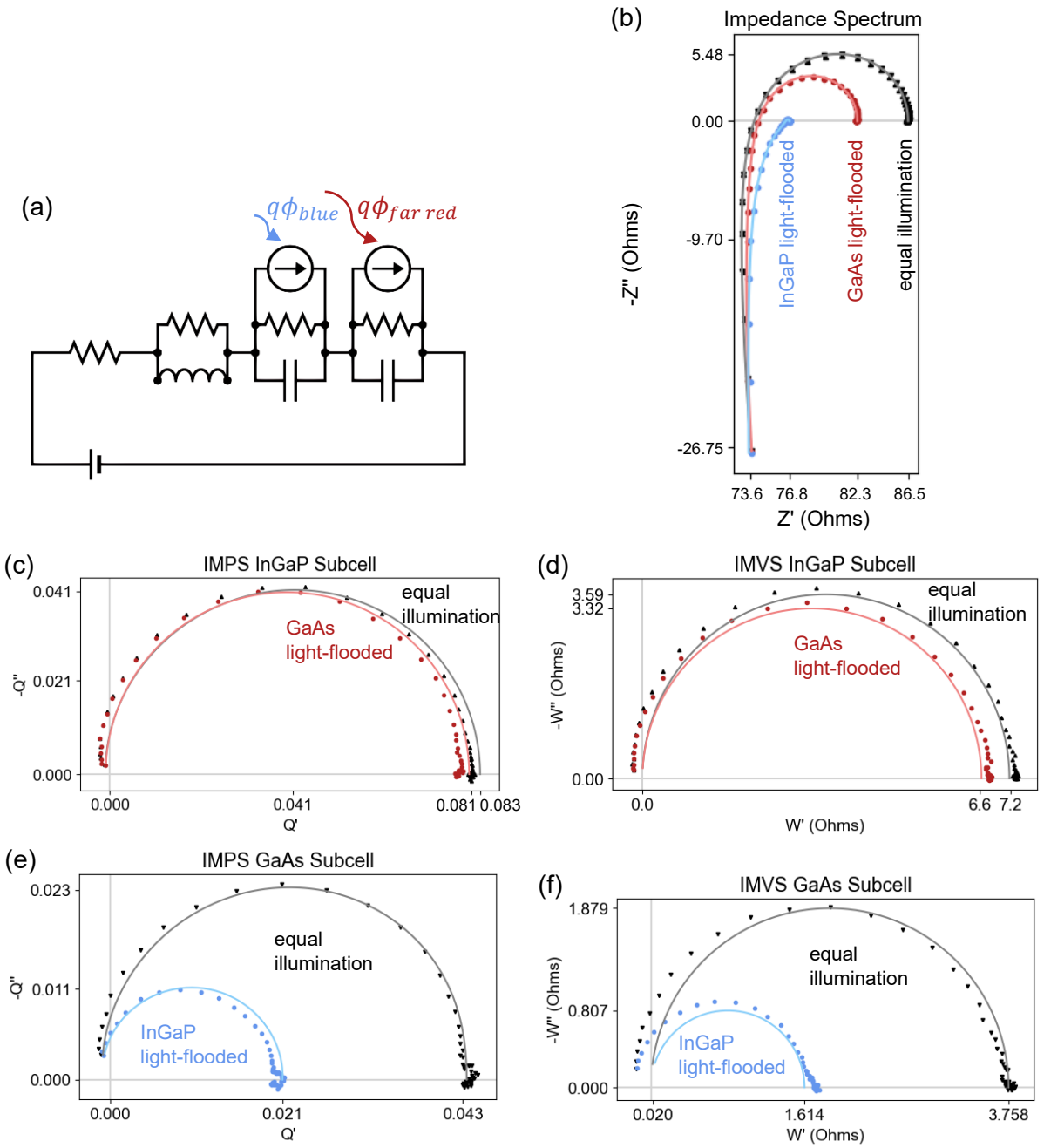

Figure 6. (a) The model used to fit (b) the impedance of the III-V tandem solar cell, (c) the top subcell's IMPS and (d) IMVS data, and (e) the bottom subcell's IMPS and (f) IMVS data at open-circuit voltage. Continuous graphs are generated using a curve fit of the measured data, which is displayed as individual data points. When flooding a subcell, the equivalent of 1 sun is used for illumination, whereas not flooding a subcell means it converts the equivalent of 0.1 suns of photons into free charge carriers. The frequency range is 1 MHz – 10 Hz, and the device was measured at the open-circuit voltage generated by the illumination conditions. The comparison between measured data and responses reconstructed by the combination of the other two techniques can be found in Appendix I.

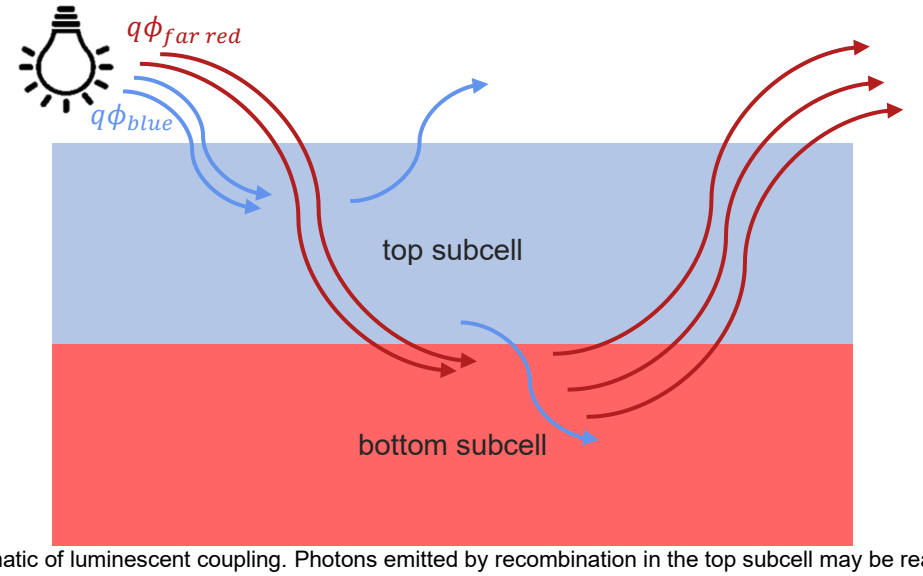

Figure 7. Schematic of luminescent coupling. Photons emitted by recombination in the top subcell may be reabsorbed by the bottom subcell but the photons emitted by the bottom subcell pass through the top subcell. This may lead to the bottom subcell generating more photocurrent when illuminating the top subcell with wavelengths outside the absorption range of the bottom subcell.

In this section, by using a III-V tandem solar cell as a blueprint, we consequently show the validity of using IMPS and IMVS to investigate subcell processes. As seen from the measurements performed on the top subcell, the impacts of the subcells on the impedance overall can be distinguished in a similar manner to light-flooding. Furthermore, the negative effects of a change in operating point are avoided using the small-perturbation techniques. This finding is especially crucial when considering more complicated systems, such as perovskite, where a change in operating conditions may impact the operating point, for example, due to ion migration [48]. Lastly, from the shape of the IMPS graphs, we can confirm that the impedance is (mostly) caused by recombination. A more detailed analysis, including the contributions of recombination and transport in the III-V TSCs can be found in Appendix J.

5 Small-Perturbation Measurements on a Perovskite/Silicon Tandem Solar Cell

As seen in section 4, IMPS and IMVS offer many advantages for characterizing subcells compared to light-flooding and impedance spectroscopy. Thus, we use this new method to characterize a perovskite/silicon TSC, which has more complex dynamics due to the properties of the perovskite [7,8,27,42,48].

5.1 Comparing Selective Subcell Light-Flooding for Characterizing Individual Processes

In the impedance response of the perovskite/silicon TSC, we observe three processes (see Figure 8). As seen in section 4, luminescent coupling may play an adverse role in accurately characterizing the bottom subcell when flooding the top subcell. Thus, we first increase the illumination of the perovskite to investigate if the perovskite's emissivity or other processes might impact the operating point (see Figure 8).

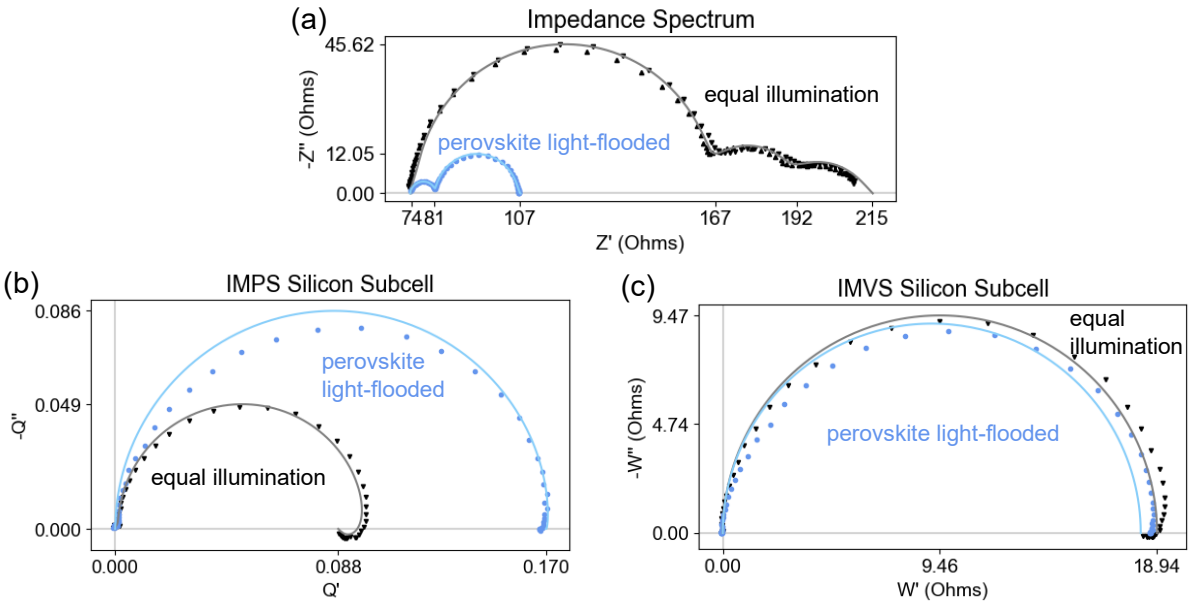

Figure 8. Comparison of data of (a) the impedance spectrum of the perovskite/silicon tandem solar cell and its (b) IMPS and (c) IMVS responses when light-perturbing the silicon subcell. Under equal illumination, both subcells generate the same amount of photocurrent as under 0.1 sun illumination. In contrast, when flooded, the top subcell generates the same amount of photocurrent as under 1 sun. The frequency range is 1 MHz – 1 Hz, and the device was measured at the open-circuit voltage generated by the illumination conditions. Comparisons of measured data and the data reconstructed from the other two perturbation measurements can be found in Appendix K.

The high- and low-frequency arcs decrease when light-flooding the perovskite, suggesting that these two processes correspond to the perovskite subcell. In contrast, the middle medium-frequency arc remains constant (see parameter values in Appendix L), suggesting that it corresponds either to contacts or the bottom subcell. From the IMVS response, though, it can easily be concluded that the latter is the case, as it reveals a recombination process with the same characteristic frequency as the middle impedance arc. This observation also supports the finding that the first and third impedance arcs are not silicon-related as they do not appear in the IMVS data. Furthermore, the IMVS data reveals that the bottom subcell is not affected by the increased illumination of the top subcell as W is unaffected by the change in blue-light intensity. Thus, we can assume that the perovskite is less emissive than the InGaP subcell of the III-V TSC.

From the IMPS response, though, we see another adverse effect of measuring a subcell by flooding the other: If the inactive subcell has significant impedance under regular operating conditions, it will hinder the charge extraction of the measured subcell. However, by flooding the inactive subcell, this resistivity is greatly underestimated, as the abundance of free charge carriers greatly reduces the resistance of the inactive subcell [21]. This effect is reflected in the IMPS data, which shows that the perovskite subcell under equal illumination prevents half of the photogenerated charge carriers from being extracted from the silicon compared to when the perovskite is illuminated with 10 times the number of photons as the bottom subcell. This large difference can be ascribed to the fact that the perovskite's impedance is far larger than that of the silicon, as seen when comparing the perovskite arcs to the silicon arc in the impedance spectrum (see Figure 8). Therefore, under regular operating conditions, the perovskite will impede the extraction of the photogenerated charges in the silicon to a far greater degree than if its impedance is decreased by light-flooding.

A similar effect, though to a lesser degree, can be observed when investigating the perovskite subcell under equal illumination and light-flooding of the silicon subcell (see Appendix M). Despite the decreased effect of light-flooding the silicon subcell on the perovskite's performance, the individual contributions of the subcells become even more clear: Since the silicon subcell has a lower characteristic frequency, its dampening effect on the

perovskite only appears for the frequencies equal to and lower than those at which the silicon arc appears. Thus, the perovskite arcs remain relatively unchanged when light-flooding the silicon, but the negative response corresponding to the silicon's behavior decreases, leading to an overall increased current response in the perovskite subcell.

From investigating the perovskite subcell under equal illumination by perturbing the blue LED, we observe a similar phenomenon in the second quadrant of the IMPS and IMVS responses as with the single-junction perovskite solar cell in section 3.1.2 (see Figure 5 and Figures 9a and b). In contrast to the bottom subcell, the top subcell's impedance is not only given by recombination but also by transport. Thus, we use three R-C pairs, to describe the perovskite subcell to incorporate the electronic and ionic recombination, as well as the transport resistance (see Figure 9c). We also add a PCE to capture the broadness of the low-frequency arc, further allowing us to quantify the ionic diffusion.

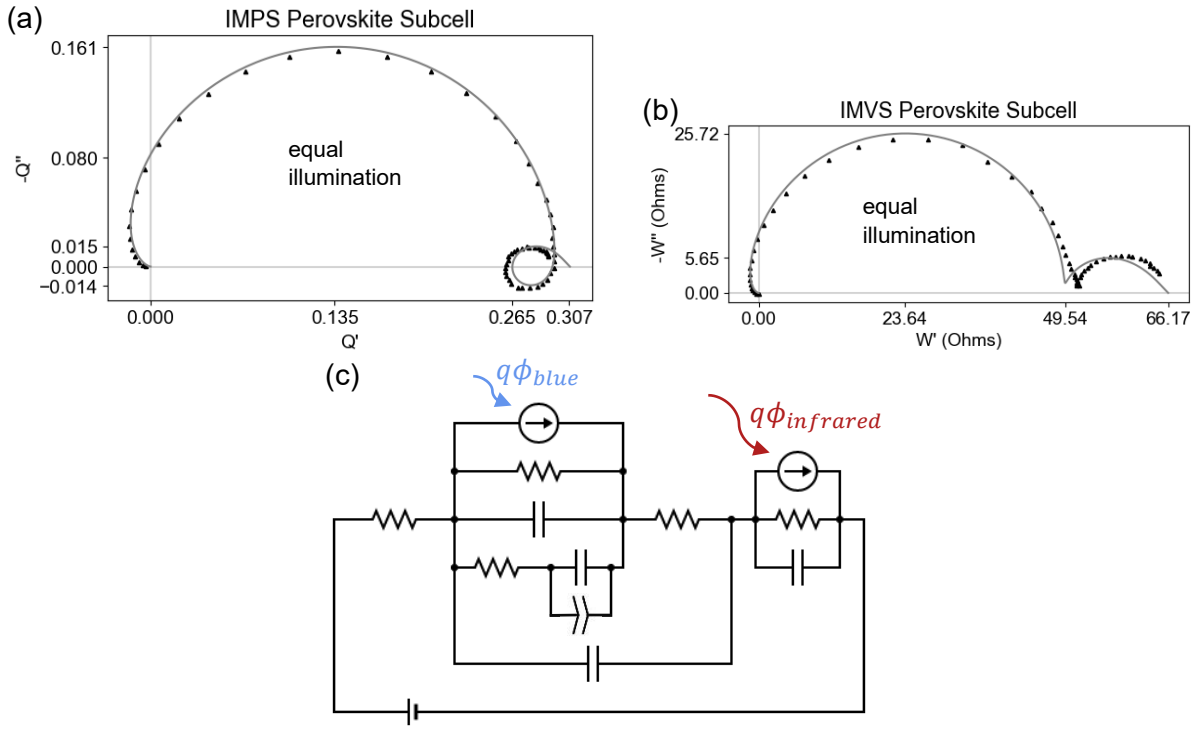

Figure 9. (a) IMPS and (b) IMVS responses of the perovskite subcell of the perovskite/silicon tandem solar cell, leading to (c) the equivalent circuit describing the full device. The device was measured over a frequency range of 1 MHz - 1 Hz at open-circuit voltage while illuminated at an equivalent to 0.1 suns. Comparisons of measured data and the data reconstructed from the other two perturbation measurements can be found in Appendix K.

5.2 Measuring and Quantifying Degradation

From the constructed model for perovskite/silicon TSCs, we can quantify the resistances and capacitances of the various processes. Thus, by comparing measurements of samples with different properties, this method lends itself to utilization as a diagnostic tool for improving solar cells by pinpointing how different behaviors may change due to internal or external factors. As a proof of concept, we compare the data of the perovskite/silicon TSC from section 5.1 (see Figures 8 and 9) to measurements performed on the same device 18 days prior (see Figure 10, Appendix N, and Table 2). Between the two sets of measurements, the device was stored in the dark in a nitrogen-atmosphere glovebox.

By comparing the subcell responses to the perturbations at V_{OC}, we see that aging leads to an increase in all resistances. However, we observe that the perovskite subcell resistances roughly triple, whereas the silicon recombination resistance increases by less than half. This development supports the notion that perovskite is far more unstable than silicon [49], as it clearly is more affected by the passage of time. It also leads to a clear decrease in

the full TSC's voltage (see Appendix O). As we can assume that this effect is (mostly) caused by the change in the perovskite's voltage, it may offer an explanation as to why not only the ionic and transport resistance – the main drivers of perovskite degradation [27,48] – but also electronic resistance (albeit to a lesser extent) has increased (see Table 2).

Although one might expect the silicon subcell not to change at all, as it can remain stable for decades [50], one could expect that the changes in internal voltage of the perovskite may affect the voltage of the silicon. Thus, despite the material being unchanged, the measurement might be at a different voltage, leading to an altered subcell response at V_{OC} (see also section 4), which may explain the increase in resistance and decrease in EQE_{diff} and η_{ext} (see Table 2).

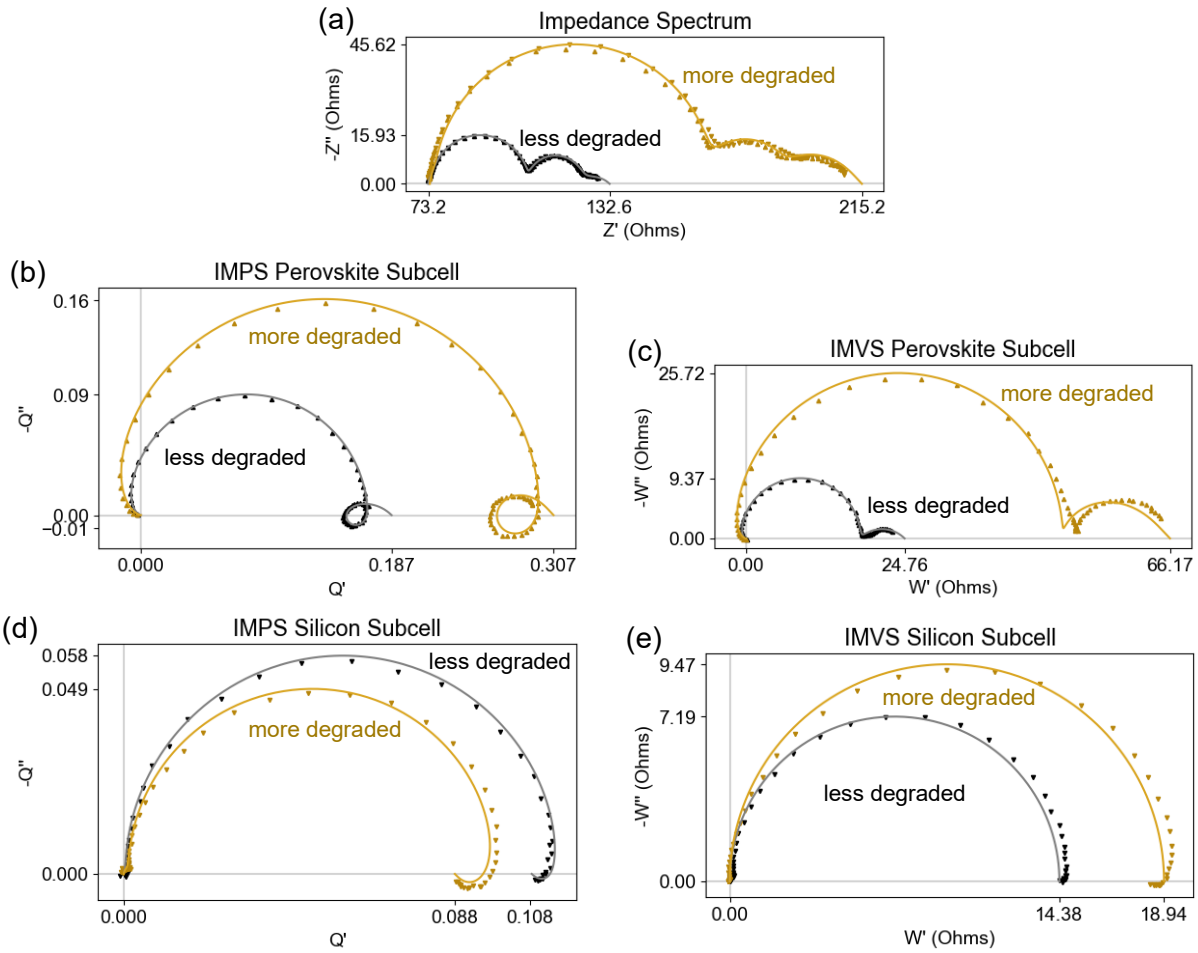

Figure 10. (a) Impedance of the perovskite/silicon tandem solar cell, its (b) IMPS and (c) IMVS responses when light-perturbing the perovskite subcell, and its (d) IMPS and (e) IMVS responses when light-perturbing the silicon subcell. The more degraded data is the same as the equal-illumination data displayed in Figures 8 and 9, whereas the less degraded data was taken from the same sample 18 days prior. In both data sets, the device was measured over a frequency range of 1 MHz - 1 Hz at open-circuit voltage while illuminated at an equivalent of 0.1 suns.

Table 2. Parameter values of the perovskite/silicon tandem solar cell (left) before and (right) after storage in a glovebox for 18 days. The characteristic times τ are found following [45]. The subscript "s" denotes series.The subscripts "Pvk" and "Si" refer to the perovskite and silicon subcells, respectively. The subscript "rec" stands for recombination, with the following abbreviations "ele" and "ion" describing the nature of the recombination as electronic and ionic, respectively. The subscript "tra" means transport. The errors are the standard deviations from the curve fits after being rounded up, with those for τ, EQE_{diff}, and η_{ext} found via error propagation, using $Eq.3$ for the former, and the equation for Q $(Eq.7)$ with DC values for the latter two. The values for the absorption efficiency are based on reflection measurements at the University of Potsdam [46]. The illumination of both subcells is equivalent to 0.1 suns, and the frequency range is 1 MHz - 1 Hz. The corrected parameters are found using simulations of the system without the series resistance added by the measurement instrument (see Appendix N).

Parameter (units)	Less Degraded	More Degraded
R_s (Ω)	73.2 ± 0.2	73.7 ± 0.4
R_s, corrected (Ω)	1.1 ± 0.2	1.6 ± 0.4
$R_{Pvk,rec,ele}$ (Ω)	36.5 ± 0.4	102 ± 2
$C_{Pvk,rec,ele}$ (nF)	119 ± 5	49 ± 5
$\tau_{Pvk,rec,ele}$ (μs)	4.3 ± 0.2	5.0 ± 0.6
$R_{Pvk,rec,ion}$ (Ω)	94.2 ± 2	300 ± 7
$C_{Pvk,rec,ion}$ (μF)	9 ± 5	31 ± 2
CPE_{Pvk} $(mF * s^{-0.5})$	1.97 ± 0.09	0.21 ± 0.02
$\tau_{Pvk,rec,ion}$ (ms)	35 ± 3	13.3 ± 0.8
$R_{Pvk,tra}$ (Ω)	6.30 ± 0.3	16.1 ± 0.9
$C_{Pvk,tra}$ (nF)	133 ± 5	81 ± 5
$\tau_{Pvk,tra}$ (μs)	0.84 ± 0.05	1.3 ± 0.2
$R_{Si,rec,ele}$ (Ω)	16.6 ± 0.2	23.8 ± 0.3
$C_{Si,rec,ele}$ (μF)	52.1 ± 0.3	25.5 ± 0.3
$\tau_{Si,rec,ele}$ (μs)	0.865 ± 0.008	0.61 ± 0.02
$EQE_{Pvk,diff}$ (%)	18.7 ± 0.3	30.7 ± 0.9
$EQE_{Pvk,diff}$, corrected (%)	41.0 ± 0.8	46 ± 2
$\eta_{Pvk,abs}$ (%)	88.6	88.6
$\eta_{Pvk,sep}$ (%)	76.6 ± 0.7	73.5 ± 0.9
$\eta_{Pvk,ext}$ (%)	27.5 ± 0.4	47 ± 2
$\eta_{Pvk,ext}$, corrected (%)	60.4 ± 0.9	71 ± 2
$EQE_{Si,diff}$ (%)	10.8 ± 0.2	8.80 ± 0.2
$EQE_{Si,diff}$, corrected (%)	23.8 ± 0.5	13.2 ± 0.3
$\eta_{Si,abs}$ (%)	95.1	95.1
$\eta_{Si,sep}$ (%)	91.1 ± 0.5	83.8 ± 0.2
$\eta_{Si,ext}$ (%)	12.50 ± 0.2	11.0 ± 0.2
$\eta_{Si,ext}$, corrected (%)	27.4 ± 0.4	16.6 ± 0.4

Contrary to expectation, η_{ext} has also increased significantly for the perovskite subcell. This does not, however, imply an increase in performance in this subcell. Instead, it is a result of the increased ratio of the perovskite's impedance versus the impedance of the full device: As the charge carriers are relatively more inhibited from recombining in the perovskite after degradation, it becomes easier to extract the free electrons generated in the top subcell. The decrease in performance also becomes especially apparent when comparing the JV curves taken at the two points in time, where the current of the degraded device is lower at any given voltage (see Appendix O).

From this section, it was observed how IMPS and IMVS can be used to quantify various electronic and optical parameters even in perovskite/silicon TSCs. Similar to single-junction devices, these techniques reveal how different transport and recombination processes, which can be hidden in impedance spectra, work in concert to contribute to the total performance and impedance of a device. From these quantifications, we can also pinpoint the extent to which a device's impedance is desirable or undesirable. Furthermore, by comparing parameter values

of different samples under different conditions, such as aging or changes in recipe, one can quantify the impact of the change in conditions on the various processes.

6 Investigating Process Behavior as a Function of Illumination and Open-Circuit Voltage

To investigate how the processes of a device may change at different voltages, the small-perturbation techniques are performed on the TSCs (see responses for the silicon photodiode and the perovskite solar cell in Appendices P and Q, respectively) with varying offset sun-equivalent illuminations to generate various V_{OC}s. From the dependence of the various resistances on the applied voltage, ideality factors for the subcells can be found [21], leading to the reconstruction of the subcells' dark currents. By additionally finding the photogenerated current using EQE_{diff} at the different voltages, the full JV response of the subcells when operating in the TSC can be found.

6.1 Results

6.1.1 III-V Tandem Solar Cell

By changing the offset intensity of the LEDs illuminating the measured device, many device parameters may change (see Appendix R and [21]). However, one may expect that values such as series resistance and η_{as} should not change with voltage. Thus, one can investigate the rigidity of the obtained parameter fits by observing to which degree the values of these parameters remain constant, as they may change to compensate for processes not captured in one's model. Thus, we use a recombination and a transport R-C pair each to describe the individual subcells (see Appendix J) as this will lead to a more constant values for R_s and η_{as}. However, we also keep η_{as} constant to the values found in Appendix J to ensure that the values for η_{ext} are not affected by errors in determining η_{as}.

In this section, we focus on two main parameter types: resistances and extraction efficiencies (see Figure 11), as they may be used to model subcell JV responses. In a single-junction solar cell, we can expect R to follow the diode equation, as the voltage will only depend on the active layer. For a TSC, one can expect the results to differ somewhat; As the full TSC's voltage $\bar{V}_{app}$ is given by

$$\bar{V}_{app} = \bar{V}_{top\ subcell} + \bar{V}_{bottom\ subcell}, \quad (Eq. 9)$$

any trend in a subcell's parameter will occur over a larger voltage range in the full TSC than in a single-junction device. Thus, when calculating the ideality factor n of a subcell using

$$R_{subcell}(\bar{V}_{app}) = R_{subcell}(\bar{V}_{subcell} = 0) * e^{-\frac{q}{n_{subcell} * k_B T} * \bar{V}_{subcell}}, \quad (Eq. 10)$$

we must therefore convert $\bar{V}_{app}$ into $\bar{V}_{subcell}$ via

$$\bar{V}_{subcell} = c_{subcell} * \bar{V}_{app}, \quad (Eq. 11)$$

where $c_{subcell}$ is the contribution of the subcell to the full TSC's voltage.

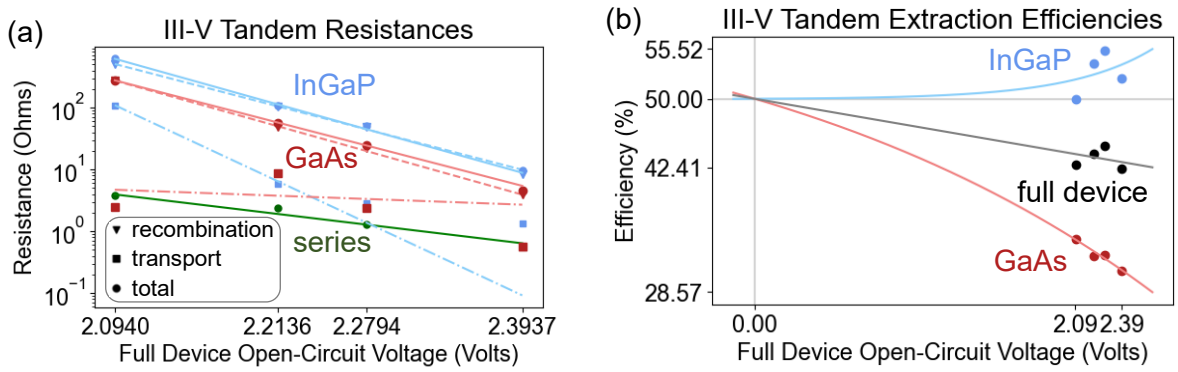

Figure 11. Developments in parameters due to using different offset light intensities of (a) resistances in the III-V tandem solar cell and (b) extraction efficiencies. The full-device extraction efficiency is assumed to be the average of the two subcells' efficiencies, with the assumption that these efficiencies are 50% at 0 V [47]. In rising order of voltage, the offset light intensities are equivalent to 0.002, 0.01, 0.02, and 0.1 suns.

Thus, we can find the ideality factors of the subcells by rewriting $Eq.10$, such that

$$R_{subcell}(\bar{V}_{app}) = R(\bar{V}_{app} = 0) * e^{-\frac{q}{n_{subcell}*k_B T}*\bar{V}_{app}*c_{subcell}}, \quad (Eq.12)$$

$$n_{subcell} = -\frac{q}{b * k_B T} * c_{subcell}, \quad (Eq.13)$$

where b is the exponent of $R_{subcell}(\bar{V}_{app})$, which can be found through curve fitting. The subcells' contributions are assumed to be proportional to one another (i.e., constant) over all voltages, with the ratio of their voltages equal to the ratio of their ideal 1-sun detailed-balance V_{OC}s. This assumption can be justified by the similarity in η_{ext}, implying the two subcells to be similar in their JV behavior in the tandem device. Using the values reported by Chen et al. [14] for the tandem devices, we thus take

$$c_{InGaP} = \frac{V_{OC,ideal,InGaP}}{V_{OC,ideal,InGaP} + V_{OC,ideal,GaAs}} = \frac{1.36\,V}{2.37\,V} = 0.574, \quad (Eq.14)$$

$$c_{GaAs} = \frac{1.01\,V}{2.37\,V} = 0.426. \quad (Eq.15)$$

Following our curve fits, we can thus find the ideality factors of the subcells to be

$$n_{InGaP} = -\frac{q}{b_{InGaP} * k_B T} * c_{InGaP} = -\frac{q}{-14.2 * k_B T} * 0.574 = 1.57, \quad (Eq.16)$$

$$n_{GaAs} = -\frac{q}{-13.1 * k_B T} * 0.426 = 1.26, \quad (Eq.17)$$

which provide insight into the (dominant) types of recombination [51] and provide insight into the shape of the (dark) JV curves of the subcells [52].

This procedure can also be repeated using only $R_{rec,subcell}$ to investigate how the ideality factors might change when assuming ideal transport (i.e. $R_{tra,subcell} = 0\,\Omega$):

$$n_{InGaP,rec} = -\frac{q}{-13.1 * k_B T} * 0.574 = 1.69, \quad (Eq.18)$$

$$n_{GaAs,rec} = -\frac{q}{-14.2 * k_B T} * 0.426 = 1.16. \quad (Eq.19)$$

We note that the ideality factor of the GaAs subcell would decrease as a result of lowered transport resistance, implying relatively more radiative recombination [51]. Issues with transport may arise due to (too) low carrier lifetimes and trapping defects, limiting extraction. As the resulting recombinations occur non-radiatively [53], a lowering of n in response to decreased R_{tra} aligns with expectations.

In contrast, the InGaP subcell's ideality factor is implied to increase as a result of less transport. This result makes little sense due to the reasoning explained above. However, one can assume that this may be caused by the curve fit, as the low-voltage point seems to be

greatly skewing the curve fit for $R_{GaAs,tra}(\bar{V}_{app})$. Assuming that the slope of $R_{GaAs,tra}(\bar{V}_{app})$ is closer to that of the higher-voltage data points, the value for $b_{GaAs,tra}$ would be much lower, implying that the GaAs subcell's transport resistance negatively impacts photoluminescence quantum yield, and thus increases the subcell's overall ideality factor.

Aside from indicating the recombination mechanisms in a solar cell, ideality factors are also useful to determine the reverse-bias saturation current

$$J_0 = \frac{k_B T}{q * R(\bar{V} = 0)} * n \quad (Eq. 20)$$

of the diode equation without illumination

$$J_{dark} = J_0 \left(e^{\frac{q}{n * k_B T} * \bar{V}} - 1 \right). \quad (Eq. 21)$$

Thus, we can calculate not only J_0 for the individual subcells – with and without transport resistance – but also simulate J_{dark}.

To complete a subcell JV analysis, the remaining variable to be found is the photogenerated current J_{light} which depends on the EQE and the incident photon current as given by

$$J_{light} = EQE * q\phi. \quad (Eq. 22)$$

From our measurements, we know that η_{ext} and, thus, EQE_{diff} have a voltage dependence (see Figure 11). Assuming that $EQE_{diff}(\bar{V}_{app})$ is constant with respect to the incident light, we thus can simply substitute EQE in $Eq. 22$ with $EQE_{diff}(\bar{V}_{app})$. To extrapolate $EQE_{diff}(\bar{V}_{app})$ to other voltages, we fit the measured data to a second diode equation, with $EQE_{diff}(\bar{V}_{app} = 0\,V)$ equal to the subcell EQEs measured by Fraunhofer ISE [54] divided by two. This halving is done to compensate for the effect of recombination in the recombination layer, since each subcell can at most contribute half a charge carrier in an operating 2J TSC. To simulate $EQE_{diff}(\bar{V}_{app})$ for the full device, the average of the two subcells' EQEs is thus taken.

From these additional curve fits, we can find the total extracted current J as the sum of the dark and light currents (see Figure 12):

$$J = J_{dark} + J_{light}. \quad (Eq. 23)$$

To simulate the individual subcell JVs as separate devices, $EQE_{diff}(\bar{V}_{app})$ is converted to $EQE_{diff}(\bar{V}_{subcell})$ using $Eq. 11$, with

$$EQE_{diff}(\bar{V}_{subcell} = 0\,V) = 2 * EQE_{diff}(\bar{V}_{app} = 0\,V) \quad (Eq. 24)$$

to compensate for the recombination layer.

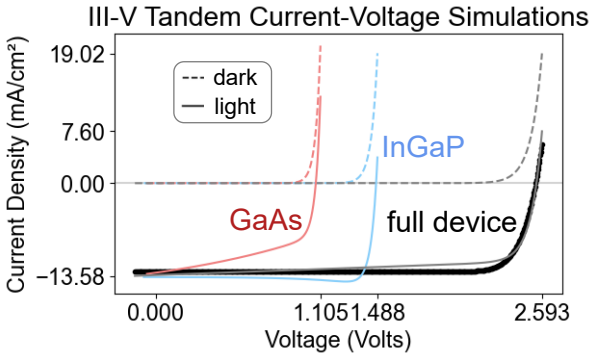

Figure 12. Simulations of subcell and full-device JV curves in dark and in 1-sun conditions (pale, thin lines) compared to a measurement of the tandem solar cell under 1-sun illumination (dark, thick line).

We observe a strong match between the measured and simulated 1-sun JV curves for the full device. Only as the voltage of maximum power (V_{MPP}) is approached does our simulation predict lower currents than what is measured. This effect seems mainly to be

caused by J_{light}, which leads to a strongly decreasing photogenerated current in the GaAs subcell, affecting the device's overall performance. Curiously, this effect seems to be somewhat offset by the InGaP subcell, which sees an increase in photogenerated current until V_{MPP} when operating in the TSC.

The reason behind this diverging behavior is unknown, though an explanation could be a faulty simulation of the dark currents. Such an inaccurate extrapolation of J_{dark} might be caused by the limited range of voltage measured. From our curve fits, it is implied that the resistances at J_{SC} are in the order of magnitude of 10^{15} Ω, which is not physically feasible. Based on the η_{ext} results (see Figure 11), one might infer that the dark current for the InGaP subcell should increase more quickly with subcell voltage than simulated, with the opposite for the GaAs subcell. This would explain the increase in η_{ext} observed in the top subcell: J_{light} would thus increase as compensation of the dark current, allowing current matching of the total subcell currents in the full tandem device.

6.1.2 Perovskite/Silicon Tandem Solar Cell

When trying to analyze the perovskite/silicon TSC in the same manner as the III-V TSC, we encounter significant difficulties: The resistances do not follow a clear trend across the full TSC's voltage (see Figure 13). As we expect the trend for $R_{subcell}(\bar{V}_{subcell})$ to be uniform, this implies that the subcell voltage contributions are not constant in this case. Based on the changes in relative resistance trends, where the perovskite subcell has a relatively smaller slope than the silicon subcell at lower voltages, but a larger one at higher voltages, we can infer that the contribution of the perovskite subcell's voltage change decreases at lower TSC voltages. If the relative subcell voltage increase truly is smaller at lower voltages, this would mean that the low-voltage resistance values would be spaced more closely to one another in $\bar{V}_{subcell}$ than in $\bar{V}_{app}$, leading to a more uniform trend for $R_{subcell}(\bar{V}_{subcell})$.

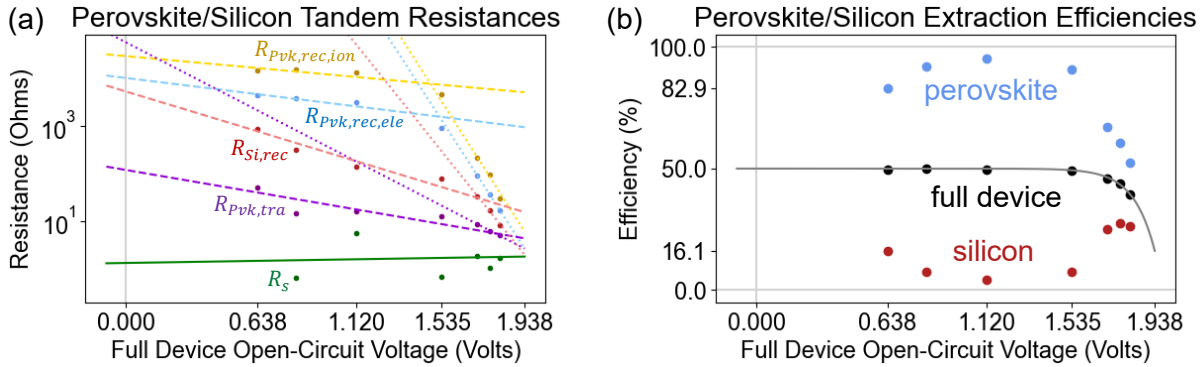

Figure 13. Developments in parameters of (a) charge extraction efficiency and (b) resistances of the perovskite layer in the perovskite/silicon tandem solar cell due to using different offset light intensities equivalent to 0.002 – 0.2 suns.

A similar dynamic is also reflected in the extraction efficiencies. Although the full-device extraction efficiency behaves as expected from a solar cell, the subcell efficiencies behave in a more peculiar manner (see Figure 13). For $\bar{V}_{app} < 1.54\,V$, we observe that additional photogenerated current is mostly extracted out of the perovskite subcell, whereas we find (approximate) current matching in η_{ext} for $\bar{V}_{app} > 1.70\,V$. This behavior likely is linked to the trends in $R_{subcell}(\bar{V}_{app})$, as the voltage ranges with differing behaviors match. The voltage-dependent extraction efficiencies thus may offer an explanation for the trends observed for the resistances, as they reveal that the perovskite is greatly limiting the charge extraction at lower voltages, with the effect lessening around 1.6 V. This phenomenon suggests that the perovskite subcell is performing worse than the silicon subcell for this voltage range. As the device's fabrication had occurred several months prior, the perovskite may have already degraded somewhat, despite measuring before the degradation observed in section 5.2.

Based on the lowest measured voltages, though, it seems that the dynamics between the subcells for voltages lower than those measured may be similar to the high voltages, as $\eta_{Pvk,ext}$ is decreasing for lower voltages but $\eta_{Si,ext}$ is increasing. This behavior is also inferred in the device's JV response, where a noticeable kink around J_{SC} (see Appendix O) may imply a switch in which subcell is limiting the extraction of current. Since the decrease in currents after degradation for voltages above zero is caused by changes in the perovskite processes, we can thus deduce that the silicon subcell is limiting for negative voltages, whereas the perovskite subcell is limiting for higher voltages.

Therefore, it is evident that the dynamics between the perovskite and silicon subcells caused by applied voltage and illumination are complex. One could divide the responses into different regimes where one assumes a constant voltage contribution as a first-order approximation in those voltage intervals, though the real subcell behaviors may strongly differ from those reconstructions. Instead, vastly increasing the number of measured points and calculating the subcell voltages by numerical integration of W (see Appendices P and Q) may be more fruitful.

6.2 Intermediate Conclusions

In this section, we observed how IMPS and IMVS at different sun-equivalent offset light intensities can be used to evaluate the performance not only of the subcells but also of each of their processes. This can, for example, include mapping JV curves for the individual subcells. Additionally, one may observe how the subcell voltage contributions may differ at different TSC voltages. Thus, the application of light-modulated techniques may provide an insightful new avenue to explore subcell dynamics as a function of applied voltage.

7 Overall Conclusions

In this thesis, IMPS and IMVS were explored as a new method for characterizing TSC subcell processes. This was achieved by first recreating the method on single-junction devices based on known procedures and exploring the interactions between impedance spectroscopy and the light-modulated techniques. Next, a III-V TSC was used to validate the application of the techniques for subcell characterization, as this device class provides a stable and simple blueprint that is easy to analyze. As perovskite-based devices are more complicated due to the presence of ions, a perovskite/silicon TSC was then measured, quantifying the effect of various processes and the changes in their behavior after degradation. Lastly, the devices were measured at different sun-equivalent illuminations to observe the voltage-dependency of the different processes, culminating in the ability to reconstruct JV curves based on measured or theoretical parameter values.

Over the span of the different sections in this thesis, we were thus able to show that IMPS and IMVS have a clear advantage over light-flooding and impedance spectroscopy for characterizing TSCs. Not only do they fulfill the goals for which the status quo methods have been developed, but they also paint a more accurate picture of the impact of transport and recombination on TSCs' performance. Additionally, these light-based techniques provide insights into some optical characteristics, such as the differential EQEs and extraction efficiencies of the subcells. Furthermore, the interactions between the two subcells under different relative illumination conditions, such as their impacts on each other's extraction efficiencies and JV characteristics of each subcell in the TSC, were explored in depth. These tests especially highlighted the drawbacks that luminescent coupling or changing photoresistivity may have on accurately determining the behavior of a subcell.

8 Discussion and Recommendations for Future Experiments

Despite some of the clear conclusions drawn in this thesis, some measurement conditions could be improved to enhance the quality of the data and its analysis. Firstly, the internal resistor of the measurement instrument affects our IMPS results. Although these could be compensated by simulating Q without this internal resistance, a more accurate picture would be obtained if the measurements are not affected by the instrument.

Due to instrument limitations, it was also not possible to measure IMVS at any voltage other than V_{OC}. Thus, the operating point was dependent on the V_{OC} generated by the illumination. Ideally, different voltages would be measured at 1-sun illumination to generate data even closer to standard operating conditions. One could still achieve this by only measuring impedance and IMPS, though this would mean not being able to check for the coherence between measurements by using the inherent mathematical relation between the three transfer functions (see $Eq. 6$). Since this check is crucial for having reliable data [29], we decided to forfeit the ability to measure at voltages other than V_{OC}, as varying illumination to change the operating voltage should not greatly change the device's behavior. Ideally, though, this tradeoff would not have to be made. With access to instrumentation that allows measurements at operating points other than V_{OC}, it would be useful to measure the TSCs also at J_{SC} or the voltage of maximum power. Thus, one could compare the effects of light-flooding to equal-illumination measurements to, for example, EQE or photoluminescence measurements also carried out at J_{SC} to draw an even stronger comparison to the status quo methods.

Additionally, it was not possible to perturb multiple LEDs with matching photon currents due to the instrument's limitations, which might have added useful reference data to which the subcell data could be compared. Although these measurements would likely not provide many new insights, it could be interesting to see if the full TSC would provide a different response than if the subcells were simply added together.

To further increase the understanding of the effect the subcells have on each other's charge extraction, one could repeat the measurements on the TSCs with a large perturbation. Analyzing the relationship between the illumination and extracted current that leads to one data point in Q, one can better understand how current extraction is affected for various degrees of illumination mismatching. As our measurements suggest that a current mismatch does not imply a full blocking of excess photogenerated charges, it would be useful to investigate the rigidity of extraction blocking in more detail. This research could also be carried out by only slightly changing the offset illumination of one subcell, which would also produce impedance data and circumvent the issue of non-linearity stemming from large perturbations.

Furthermore, it may be beneficial to obtain cleaner data on the III-V TSC due to their imperfect measurements, as seen in the mismatch of Z and W/Q (see Appendix I). Assuming that the IMPS data is not fully accurate, we would expect a smaller response in Q for the top subcell under equal illumination compared to light-flooding, as the increased resistance from the bottom subcell would block some charge extraction, as seen in the perovskite/silicon TSC (see Figure 9). Similarly, the data under light-flooding is not fully reliable, as a change in the offset current was observable, despite the offset voltage remaining constant (see Appendix T). Although these drawbacks affect the data evaluation somewhat, the overall insights of the comparison between equal illumination and light-flooding in section 4 remain valid. Nevertheless, the conclusions would bear more weight with more accurate data.

When remeasuring the TSCs, one might also consider extending the range of sun-equivalent illuminations to measure a larger span of voltages. From these measurements, more accurate trends, especially for the perovskite/silicon TSC, might be observed, providing

clearer insights into the subcell dynamics. Similarly, one could investigate the obtained IMVS data further by converting W into a V_{OC} for each subcell by integrating W by the input photocurrent perturbation (see results for the silicon photodiode and perovskite solar cell in Appendices P and Q, respectively). Ideally, this would be done numerically from a larger number of data points, as creating a physically accurate curve fit for the extraction efficiencies can prove to be very challenging. This approach may also provide clearer insights into the voltage-dependence of the voltage contributions of the subcells. To check for the validity of the findings, one could then compare the results with electroluminescence measurements, which can also reveal the subcells' V_{OC}s [14,15]. From this analysis, one could get stronger insights into how the subcells contribute to the overall device. Thus, this analysis would add to the benefits of small-perturbation techniques.

Finally, further behaviors can be studied by expanding the applied methods or measuring a triple-junction TSC. For example, intensity-modulated photoluminescence spectroscopy [61] may offer insightful new data. This technique could especially be useful when applied to TSCs, as it may quantify the strength of the luminescent coupling between the devices subcells. Similarly, the understanding of TSCs could be expanded by measuring triple-junction devices, which may display even more complex interactions between their three active layers, such as coupling resistances (see Appendix B) specific to two adjacent subcells. The connection between coupling resistances and the recombination layer may also be further explored by characterizing TSCs fabricated purposefully with good-performing and poor recombination layers.

9 Methods

9.1 Materials and Equipment Used

All small-perturbation measurements were performed using Fluxim's Paios. The silicon photodiode used was the one integrated in Fluxim's test print circuit board. The perovskite solar cell was fabricated at the University of Potsdam, whereas the TSCs were fabricated at the Fraunhofer Institute for Solar Energy Systems (ISE). To adapt the measurement setup to the different samples, we designed 3D parts with Onshape to be printed out with PLA using the Creality K1C 3D printer.

The LEDs used during the small-perturbation measurements were the blue and far-red XP-E2 LEDs by CREE LED, as well as the infrared OCI-490-20 ID980 LED by EPIGAP OSA. For IMPS and IMVS, the light-intensity modulation was carried out using the Paios. For the experiments requiring two LEDs, the unperturbed LED was powered using a Keithley 2401 source-measuring unit. To ensure homogeneity of the illumination, a UVFS ground glass diffuser (220 grit) by ThorLabs was used. To make the infrared and far-red LEDs have similar brightness at equal input currents as the blue LED, they were each covered with a few layers of tissue paper, which further added to the homogeneity of their light emission.

To measure the JV curves, the G2V Pico and the Keithley were used. To ensure that the Pico's output was consistent with expectations, its power output was confirmed both with a calibrated test photodiode and with a PM100D power meter by ThorLabs for individual LEDs.

Aside from the reflection measurement performed with the UV/Vis by Perkin Elmer, all measurements were performed inside a nitrogen-atmosphere glovebox. The water and oxygen values were usually around 0.1 ppm.

9.2 Small-Perturbation Techniques

All measurements were performed at V_{OC}. The maximum frequency was 1 MHz, whereas the lowest frequency was 10 Hz, 1 Hz, and 316 mHz, for the silicon photodiode and the III-V TSCs,

the perovskite/silicon TSCs, and the perovskite single-junction solar cell, respectively. The perturbations were small enough to elicit a linear response, as was checked by analyzing the raw data of the applied and measured perturbations (examples see Appendix T). To ensure that the measurements had constant $\bar{V}_{app}$ and $\bar{J}_{app}$, the raw data for the two values was checked (examples see Appendix T). To ensure the system was stable, each set of measurements was repeated until no changes between the results were observable. For the light-flooding experiments, the light-flooded subcell was illuminated with the equivalent of 1 sun, whereas the other subcell had an offset illumination equal to 0.1 sun. When varying in illumination of the TSCs, both LEDs' brightnesses were changed such that both subcells were always illuminated equally.

9.3 Calibrations

The Paios can calibrate impedance caused by cables and internal resistors automatically using the photodiode testprint supplied with the instrument. This correction is applied to the impedance spectroscopy measurements, but it does not transfer to IMPS. Thus, to create coherence between the two measurements, the resistance of 72.1 Ω due to the cables and the Paios is added to the impedance data for the data evaluation in this thesis.

The LEDs can also be calibrated somewhat automatically by the Paios using the LED Calibration function in the Paios Hardware Manager tab: The instrument can adjust its internal parameter for LED output intensity, which is used for light-dependent measurements. By measuring the current produced in the testprint photodiode from different LED currents, the instrument can match its LED intensity values to scale linearly with LED photoemission. Thus, halving the Paios's LED intensity parameter will lead to a current input to the LED such that the resulting photoemission is halved as well.

The actual photoemission for a given output intensity, however, is not known. Thus, the instrument's intensity parameter, which is also used by the Paios software to normalize the current and voltage output from IMPS and IMVS as given by $Eq.21$ and 22, needs to be converted to the LEDs' photocurrent densities when reaching the measured sample. Furthermore, the LED emissions need to be related to the solar spectrum to ensure that our measurements can simulate solar operating conditions by creating the same ratio of free charges between TSC subcells as they would when illuminated by the sun.

$$Q_{Paios} = \frac{\tilde{J}_{ext} * A_{device}}{\widetilde{intensity}_{LED,Paios}}, \quad (Eq.21)$$

$$W_{Paios} = \frac{\tilde{V}_{app} * A_{device}}{\widetilde{intensity}_{LED,Paios}}. \quad (Eq.22)$$

To determine the emitted photon current of the LEDs used for the intensity-modulated techniques and relate it to solar radiation, several data sets needed to be taken into consideration. Firstly, a photodiode needed to be calibrated to determine its EQE for the given LED spectra. As the EQE is given by

$$EQE = \frac{J_{PD}}{J_{\phi,LED}}, \quad (Eq.23)$$

where J_{PD} is the extracted current density from the photodiode and $J_{\phi,LED}$ is the photocurrent density emitted by the LED, defined as

$$J_{\phi,LED} = \#_{ph} * q * A_{PD}^{-1} * s^{-1}, \quad (Eq.24)$$

with $\#_{ph}$ being the number of photons reaching the photodiode, q the elementary charge, A_{PD} the area of the photodiode, and s the unit seconds.

Thus, the next step entailed finding the number of photons, which is given by the ratio of the energy of the LED's photoemission hitting the photodiode in the span of a second and the energy of a single photon:

$$\#_{ph} = \frac{E_{\phi,LED}}{E_{ph}}. \quad (Eq. 25)$$

The photoemission's energy can be found using its known intensity $I_{\phi,LED}$ by considering that energy is power $P_{\phi,LED}$ multiplied by time, which in turn is equal to intensity multiplied by the area of the photodiode and time. Meanwhile, the energy of a photon can be rewritten into the known average wavelength λ_{ph} as the Planck constant h multiplied by the speed of light c, divided by wavelength. Thus, we arrive at

$$\#_{ph} = \frac{P_{\phi,LED} * s}{h * c/\lambda_{ph}}, \quad (Eq. 26)$$

$$= \frac{I_{\phi,LED} * s * A_{PD}}{h * c/\lambda_{ph}}. \quad (Eq. 27)$$

Plugging this into our expression for $J_{\phi,LED}$ in $Eq. 24$ yields

$$J_{\phi,LED} = \frac{I_{\phi,LED} * s * A_{PD}}{h * c/\lambda_{ph}} * q * A_{PD}^{-1} * s^{-1}, \quad (Eq. 28)$$

$$= \frac{I_{\phi,LED}}{h * c/\lambda_{ph}} * q, \quad (Eq. 29)$$

such that the EQE of the photodiode can be found. The EQE values at -5 V were found to be around 29%, 95%, and 100% for the blue, far red, and infrared LEDs, respectively.

To find the photoemission of the different LEDs at a given intensity, the current output of the photodiode at -5 V was recorded for the various LEDs. To account for the inhomogeneity of the photoemission, the current was recorded for various locations on the Paios, such that the same areas as the different samples used for the measurements were mapped out. For the larger samples, to find the overall photoemission, the average of the recorded photodiode's current at the different locations was thus used. As these measurements directly relate photoemission to the Paios's output intensity parameter, this allows for the conversion of Q_{Paios} and W_{Paios} into Q and W by multiplying them by

$$\frac{Q}{Q_{Paios}} = \frac{\tilde{J}_{ext}/\tilde{J}_{\phi,LED}}{\tilde{J}_{ext} * A_{device}/\widetilde{intensity}_{LED,Paios}}, \quad (Eq. 30)$$

$$= \frac{\widetilde{intensity}_{LED,Paios}}{\tilde{J}_{\phi,LED} * A_{device}}, \quad (Eq. 31)$$

where the ratio between the Paios intensity parameter and the LED's emitted photocurrent is linear and determined.

To convert the LED spectra into sun-equivalents, the relative intensity spectra of the LEDs from the respective data sheets needed to be converted into photon current emission per wavelength. This was done by converting the relative intensity (see Figure 14a) to photocurrent density and normalizing the values (see Figure 14b) such that the integral of the spectra matched the values determined from the measurements using the photodiode. Next, the photon currents per wavelength of the LEDs were each multiplied by the EQE of the (sub)cell (see Figure 14c) and integrated to find the extracted photogenerated current caused by the blue LED (see Figure 14d). This step was then repeated with the solar spectrum (see Figures 14e and f). Knowing that the LEDs' photocurrents scale linearly with the Paios's output intensity, we could then convert the LED spectra to sun equivalents by dividing the extracted photogenerated current from the LED by the one extracted from the solar spectrum. Thus, the

LEDs could be tuned such that the TSC subcells should have the same ratio of extractable photogenerated charges as if they were operating under a solar spectrum.

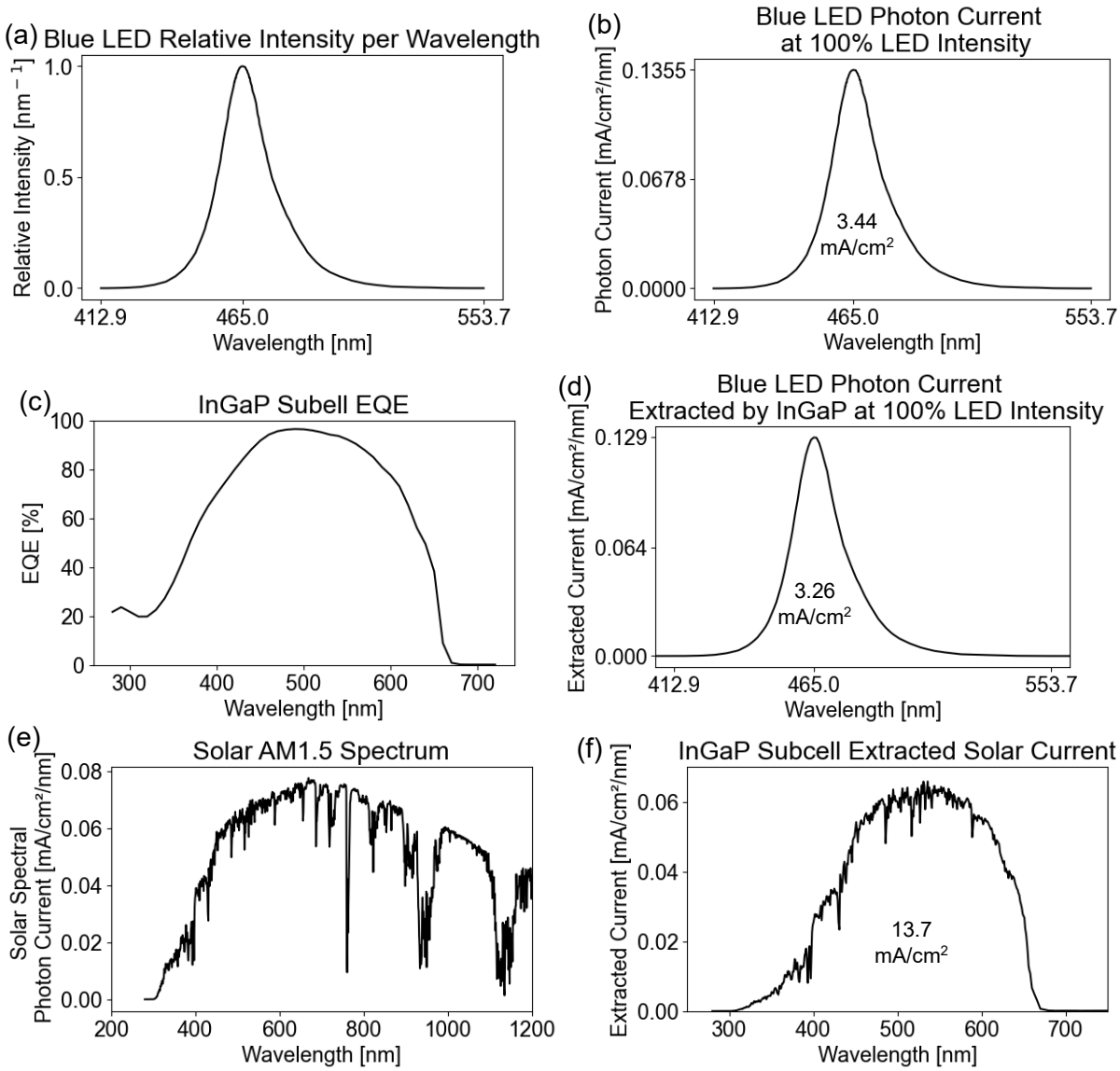

Figure 14. Steps of a subcell-specific LED calibration, as shown with the calibration of the blue LED for the InGaP subcell of the III-V tandem solar cell. (a) The relative intensity of the blue LED spectrum, obtained from the LED's data sheet [56], is converted into (b) its photon current at 100% Paios output intensity, with the total current density as the value of the integral of the spectrum written underneath the curve. This spectrum is multiplied by (c) the InGaP subcell's EQE to form (d) the extracted current per wavelength generated by the blue LED, with the total current density as the value of the integral of the spectrum written underneath the curve. (e) The solar AM1.5 spectrum [57] is also multiplied by the subcell's EQE [54] to obtain (f) the current density per wavelength generated by the sun extracted from the subcell, with the total current density as the integral of the spectrum written underneath the curve. The extracted photocurrents for all tandem subcells from the LEDs and the solar AM1.5 spectrum are found in Appendix A.

9.4 Data Evaluation

To evaluate the data gathered, Python scripts in Jupyter Notebook were used. To evaluate the impedance spectra without IMPS and IMVS for the silicon photodiode and the perovskite solar cell, the impedance.py package was used. In all other cases, a script was written that could fit Z, Q, and W simultaneously to all the desired parameters using the scipy.optimize.curve_fit package. To ensure that all data sets were weighted equally, they were normalized such that, during fitting, all values in the first quadrant of each graph were in the ranges x=[0,1] and y=[0,1]. Similarly, the other data sets were also evaluated using Python scripts and the scipy.optimize.curve_fit package when needed.

Acknowledgements

My work this past academic year was only made possible by the support I received from many truly incredible people. Firstly, I deeply thank **Bruno** for hiring me for this position and supporting me whenever I had a physics-related question, but also for encouraging me to slow down and rest when needed. Similarly, **Agustin** was an incredibly motivating daily supervisor, sharing in my excitement over new insights from measuring and modeling the devices, guiding me with many exciting conversations about possible data interpretations (for which I definitely have taken too much of his time), and cheering me on with great passion. **Moritz** also played a great part in my projects, happily stepping up as an unofficial, second supervisor so I could also turn to him when I felt I had already asked Agustin enough questions for the day. From a technical point of view, my project also would have been impossible without the amazing help from **Alexander** and **Marc**. Between Alexander's amazing electronic support, creating circuit boards and helping Agustin, Moritz, and me trouble-shoot the Paios (which certainly was no easy task!), as well as Marc's ever-present readiness to provide me with materials and answering all my questions about the lab with great patience, I could not have been in more capable hands.

Furthermore, the rest of my research group was also a great joy to work with. I will always cherish **Larissa** for her positive attitude and outlook, as well as the random noises and stares we have exchanged (I swear it helps with thinking!). My deep appreciation also goes to **Jeroen** for being such a kind and gentle soul – even though we did not talk about it afterwards, our conversation when biking back from the VU AMC meant more to me than he probably realizes. I am also thankful to **Imme** for looking out for me and for sharing fun stories about our times at AUC. With her title of senior PhD in the group passed on to **Daphne**, the scepter has been handed to another capable soul, with whom I have had the fortune to share many rants about impedance and equally, but positive, passionate conversations about food. I also appreciated sharing a passion for small engineering-type projects with **Lars**, from which I am sure I could learn many more useful, exciting skills. My thanks also extend to **Filip**, as well as the rest of my **master's cohort**, for all the mental support and checking in with me, especially as we all approached our thesis deadline. As the other fellow Gen Z geek, I have also enjoyed every conversation with **Francesco** immensely, and I look forward to seeing where our friendship may go from here. He and **Athira**, who also only recently joined AMOLF but has already contributed much both personally and academically to the group, will most certainly have a bright future in their PhD careers. I also want to thank **Paul**, **Jeong-Ju**, and **Hyeji** for the short but lovely time we shared together. Finally, in our group, my gratitude goes to the curiosity that was always expressed with great humility by **Tae-Youl** – may his light forever shine on.

Lastly, my deepest appreciation goes out to all my friends and family who have supported me throughout this journey. Naturally, I am deeply grateful for my **parents**' constant reassurance that I can always rely on them whenever needed. The same goes for my loving partner **Daan**, as well as my truly wonderful past, present, and future housemates – **Nele**, **Nora**, **Zara**, **Kristóf**, and **Isis** – who have proven time and time again that chosen family is just as important as blood relatives. Yet, I could also not have gotten where I am today without my **grandparents** granting me the privilege to pursue my dreams in academia and beyond. Lastly, a special mention goes out to the members of the **Nanoscale Solar Cells** group, especially **Sarah**, for being my gateway and reason for returning to the amazing community of AMOLF, filled with excellent people all across the different departments and support staff.

References

[1] “Annual solar module production worldwide 2022,” Statista. Accessed: Sep. 23, 2024. [Online]. Available: https://www.statista.com/statistics/668764/annual-solar-module-manufacturing-globally/

[2] NREL, “Best Research-Cell Efficiency Chart.” Accessed: Jun. 23, 2025. [Online]. Available: https://www.nrel.gov/pv/cell-efficiency.html

[3] T. Tiedje, E. Yablonovitch, G. D. Cody, and B. G. Brooks, “Limiting efficiency of silicon solar cells,” *IEEE Trans. Electron Devices*, vol. 31, no. 5, pp. 711–716, May 1984, doi: 10.1109/T-ED.1984.21594.

[4] “Net Zero by 2050 - A Roadmap for the Global Energy Sector”.

[5] *tandem solar cells - Search*, database.

[6] A. de Vos, “Detailed balance limit of the efficiency of tandem solar cells,” *J. Phys. Appl. Phys.*, vol. 13, no. 5, pp. 839–846, May 1980, doi: 10.1088/0022-3727/13/5/018.

[7] Md. H. Miah, M. U. Khandaker, Md. B. Rahman, M. Nur-E-Alam, and M. A. Islam, “Band gap tuning of perovskite solar cells for enhancing the efficiency and stability: issues and prospects,” *RSC Adv.*, vol. 14, no. 23, pp. 15876–15906, 2024, doi: 10.1039/D4RA01640H.

[8] A. These, L. J. A. Koster, C. J. Brabec, and V. M. Le Corre, “Beginner’s Guide to Visual Analysis of Perovskite and Organic Solar Cell Current Density–Voltage Characteristics,” *Adv. Energy Mater.*, vol. 14, no. 21, p. 2400055, Jun. 2024, doi: 10.1002/aenm.202400055.

[9] J. H. Park, S. K. Hwang, S. G. Ji, and J. Y. Kim, “Characterization of various tandem solar cells: Protocols, issues, and precautions,” *Exploration*, vol. 3, no. 2, p. 20220029, 2023, doi: 10.1002/EXP.20220029.

[10] D. Chojniak *et al.*, “Measuring the External Quantum Efficiency of Tandem Photovoltaic Modules Using an LED-Based Solar Simulator,” *Sol. RRL*, vol. 9, no. 1, p. 2400517, 2025, doi: 10.1002/solr.202400517.

[11] G. Siefer, C. Baur, and A. W. Bett, “External quantum efficiency measurements of Germanium bottom subcells: Measurement artifacts and correction procedures,” in *2010 35th IEEE Photovoltaic Specialists Conference*, Honolulu, HI, USA: IEEE, Jun. 2010, pp. 000704–000707. doi: 10.1109/PVSC.2010.5616919.

[12] C. Leon *et al.*, “Understanding and monitoring the capacitance-voltage technique for the characterization of tandem solar cells,” *Prog. Photovolt. Res. Appl.*, vol. 28, no. 6, pp. 601–608, Jun. 2020, doi: 10.1002/pip.3235.

[13] J. H. Park, S. G. Ji, I. J. Park, S. K. Hwang, H. W. Lim, and J. Y. Kim, “Sub-cell characterization of two-terminal perovskite/silicon tandem solar cells,” *Cell Rep. Phys. Sci.*, vol. 3, no. 10, p. 101076, Oct. 2022, doi: 10.1016/j.xcrp.2022.101076.

[14] S. Chen *et al.*, “Thorough subcells diagnosis in a multi-junction solar cell via absolute electroluminescence-efficiency measurements,” *Sci. Rep.*, vol. 5, no. 1, p. 7836, Jan. 2015, doi: 10.1038/srep07836.

[15] I. J. Djeukeu, J. Horn, M. Meixner, E. Wagner, S. W. Glunz, and K. Ramspeck, “Subcell-Resolved Electroluminescence Imaging of Monolithic Perovskite/Silicon Tandem Solar Cell for High-Throughput Characterization,” *Sol. RRL*, vol. 8, no. 19, p. 2400469, Oct. 2024, doi: 10.1002/solr.202400469.

[16] K. Jäger, P. Tillmann, E. A. Katz, and C. Becker, “Perovskite/Silicon Tandem Solar Cells: Effect of Luminescent Coupling and Bifaciality,” *Sol. RRL*, vol. 5, no. 3, p. 2000628, Mar. 2021, doi: 10.1002/solr.202000628.

[17] J. T. S. Irvine, D. C. Sinclair, and A. R. West, “Electroceramics: Characterization by Impedance Spectroscopy,” *Adv. Mater.*, vol. 2, no. 3, pp. 132–138, Mar. 1990, doi: 10.1002/adma.19900020304.

[18] A. S. Kavasoglu and H. Bayhan, “Admittance and Impedance Spectroscopy on Cu(In,Ga)Se_2 Solar Cells”.

[19] P. Yadav, K. Pandey, V. Bhatt, M. Kumar, and J. Kim, “Critical aspects of impedance spectroscopy in silicon solar cell characterization: A review,” *Renew. Sustain. Energy Rev.*, vol. 76, pp. 1562–1578, Sep. 2017, doi: 10.1016/j.rser.2016.11.205.

[20] E. von Hauff, “Impedance Spectroscopy for Emerging Photovoltaics,” *J. Phys. Chem. C*, vol. 123, no. 18, pp. 11329–11346, May 2019, doi: 10.1021/acs.jpcc.9b00892.
[21] I. Zarazua *et al.*, “Surface Recombination and Collection Efficiency in Perovskite Solar Cells from Impedance Analysis,” *J. Phys. Chem. Lett.*, vol. 7, no. 24, pp. 5105–5113, Dec. 2016, doi: 10.1021/acs.jpclett.6b02193.
[22] S.-M. Yoo, S. J. Yoon, J. A. Anta, H. J. Lee, P. P. Boix, and I. Mora-Seró, “An Equivalent Circuit for Perovskite Solar Cell Bridging Sensitized to Thin Film Architectures,” *Joule*, vol. 3, no. 10, pp. 2535–2549, Oct. 2019, doi: 10.1016/j.joule.2019.07.014.
[23] S. M. Seyed-Talebi and I. Kazeminezhad, “Performance improvement of fully ambient air fabricated perovskite solar cells in an anti-solvent process using TiO2 hollow spheres,” *J. Colloid Interface Sci.*, vol. 562, pp. 125–132, Mar. 2020, doi: 10.1016/j.jcis.2019.12.004.
[24] P. F. Betancur, O. E. Solis, R. Abargues, T. S. Ripolles, and P. P. Boix, “Recombination resistance identification through current–voltage curve reconstruction in perovskite solar cells,” *Phys. Chem. Chem. Phys.*, vol. 26, no. 48, pp. 29904–29912, 2024, doi: 10.1039/D4CP04143G.
[25] B. Roose, K. Dey, M. R. Fitzsimmons, Y.-H. Chiang, P. J. Cameron, and S. D. Stranks, “Electrochemical Impedance Spectroscopy of All-Perovskite Tandem Solar Cells,” *ACS Energy Lett.*, vol. 9, no. 2, pp. 442–453, Feb. 2024, doi: 10.1021/acsenergylett.3c02018.
[26] I. J. Park, J. H. Park, S. G. Ji, M.-A. Park, J. H. Jang, and J. Y. Kim, “A Three-Terminal Monolithic Perovskite/Si Tandem Solar Cell Characterization Platform,” *Joule*, vol. 3, no. 3, pp. 807–818, Mar. 2019, doi: 10.1016/j.joule.2018.11.017.
[27] M. C. Schmidt, E. Gutierrez-Partida, M. Stolterfoht, and B. Ehrler, “Impact of Mobile Ions on Transient Capacitance Measurements of Perovskite Solar Cells,” *PRX Energy*, vol. 2, no. 4, p. 043011, Nov. 2023, doi: 10.1103/PRXEnergy.2.043011.
[28] K. T. Tanko *et al.*, “The Roles of Ion Migration on Perovskite Solar Cell Operational Stability at Various Illumination Intensities,” *Sol. RRL*, p. 202500162, Jun. 2025, doi: 10.1002/solr.202500162.
[29] A. O. Alvarez, S. Ravishankar, and F. Fabregat-Santiago, “Combining Modulated Techniques for the Analysis of Photosensitive Devices,” *Small Methods*, vol. 5, no. 10, p. 2100661, Oct. 2021, doi: 10.1002/smtd.202100661.
[30] A. S. R. Bati, Y. L. Zhong, P. L. Burn, M. K. Nazeeruddin, P. E. Shaw, and M. Batmunkh, “Next-generation applications for integrated perovskite solar cells,” *Commun. Mater.*, vol. 4, no. 1, p. 2, Jan. 2023, doi: 10.1038/s43246-022-00325-4.
[31] I. Mosquera-Lois, Y.-T. Huang, H. Lohan, J. Ye, A. Walsh, and R. L. Z. Hoye, “Multifaceted nature of defect tolerance in halide perovskites and emerging semiconductors”.
[32] T. Dai *et al.*, “Strategies for High-Performance Large-Area Perovskite Solar Cells toward Commercialization,” *Crystals*, vol. 11, no. 3, p. 295, Mar. 2021, doi: 10.3390/cryst11030295.
[33] W. Fu *et al.*, “Stability of perovskite materials and devices,” *Mater. Today*, vol. 58, pp. 275–296, Sep. 2022, doi: 10.1016/j.mattod.2022.06.020.
[34] J. M. Frost, K. T. Butler, F. Brivio, C. H. Hendon, M. Van Schilfgaarde, and A. Walsh, “Atomistic Origins of High-Performance in Hybrid Halide Perovskite Solar Cells,” *Nano Lett.*, vol. 14, no. 5, pp. 2584–2590, May 2014, doi: 10.1021/nl500390f.
[35] D. Di Girolamo *et al.*, “Ion Migration-Induced Amorphization and Phase Segregation as a Degradation Mechanism in Planar Perovskite Solar Cells,” *Adv. Energy Mater.*, vol. 10, no. 25, p. 2000310, Jul. 2020, doi: 10.1002/aenm.202000310.
[36] L. Meng, J. You, and Y. Yang, “Addressing the stability issue of perovskite solar cells for commercial applications,” *Nat. Commun.*, vol. 9, no. 1, p. 5265, Dec. 2018, doi: 10.1038/s41467-018-07255-1.
[37] B. Wang, X. Tian, S. D. Stranks, and F. You, “Transitioning Photovoltaics to All-Perovskite Tandems Reduces 2050 Climate Change Impacts of PV Sector by 16%,”

Environ. Sci. Technol., vol. 59, no. 19, pp. 9540–9551, May 2025, doi: 10.1021/acs.est.5c00121.
[38] M. P. Vecchi, “Integrated tandem solar cells,” *Sol. Energy*, vol. 22, no. 4, pp. 383–388, Sep. 1978, doi: 10.1016/0038-092X(79)90193-2.
[39] M. de Bastiani, A. S. Subbiah, E. Aydin, F. H. Isikgor, T. G. Allen, and S. de Wolf, “Recombination junctions for efficient monolithic perovskite-based tandem solar cells: physical principles, properties, processing and prospects,” *Mater. Horiz.*, vol. 7, no. 11, pp. 2791–2809, Nov. 2020, doi: 10.1039/D0MH00990C.
[40] M. A. Steiner *et al.*, “Measuring IV curves and subcell photocurrents in the presence of luminescent coupling,” *IEEE J. Photovolt.*, vol. 3, no. 2, pp. 879–887, Apr. 2013, doi: 10.1109/JPHOTOV.2012.2228298.
[41] A. Ch. Lazanas and M. I. Prodromidis, “Electrochemical Impedance Spectroscopy─A Tutorial,” *ACS Meas. Sci. Au*, vol. 3, no. 3, pp. 162–193, Jun. 2023, doi: 10.1021/acsmeasuresciau.2c00070.
[42] E. von Hauff and D. Klotz, “Impedance spectroscopy for perovskite solar cells: characterisation, analysis, and diagnosis,” *J. Mater. Chem. C*, vol. 10, no. 2, pp. 742–761, Jan. 2022, doi: 10.1039/D1TC04727B.
[43] S. Ravishankar, A. Riquelme, S. K. Sarkar, M. Garcia-Batlle, G. Garcia-Belmonte, and J. Bisquert, “Intensity-Modulated Photocurrent Spectroscopy and Its Application to Perovskite Solar Cells,” *J. Phys. Chem. C*, vol. 123, no. 41, pp. 24995–25014, Oct. 2019, doi: 10.1021/acs.jpcc.9b07434.
[44] Y. T. Set, B. Li, F. J. Lim, E. Birgersson, and J. Luther, “Analytical modeling of intensity-modulated photovoltage spectroscopic responses of organic bulk-heterojunction solar cells,” *Appl. Phys. Lett.*, vol. 107, no. 17, p. 173301, Oct. 2015, doi: 10.1063/1.4934920.
[45] J. Bisquert and E. H. Balaguera, “Brief Guide to Transformation of Constant Phase Element Impedance to Equivalent Capacitor or Inductor,” *J. Phys. Chem. Lett.*, vol. 16, no. 23, pp. 5779–5783, Jun. 2025, doi: 10.1021/acs.jpclett.5c01131.
[46] B. Alebachew Seid, private communication, May 26, 2025.
[47] O. Höhn, private communication, Jun. 24, 2025.
[48] M. A. Torre Cachafeiro *et al.*, “Ion Migration in Mesoscopic Perovskite Solar Cells: Effects on Electroluminescence, Open Circuit Voltage, and Photovoltaic Quantum Efficiency,” *Adv. Energy Mater.*, vol. 15, no. 5, p. 2403850, Nov. 2024, doi: 10.1002/aenm.202403850.
[49] L. Duan *et al.*, “Stability challenges for the commercialization of perovskite–silicon tandem solar cells,” *Nat. Rev. Mater.*, vol. 8, no. 4, pp. 261–281, Apr. 2023, doi: 10.1038/s41578-022-00521-1.
[50] W. Oh *et al.*, “Analysis of degradation in 25-year-old field-aged crystalline silicon solar cells,” *Microelectron. Reliab.*, vol. 100–101, p. 113392, Sep. 2019, doi: 10.1016/j.microrel.2019.06.084.
[51] V. M. Le Corre, T. S. Sherkar, M. Koopmans, and L. J. A. Koster, “Identification of the dominant recombination process for perovskite solar cells based on machine learning,” *Cell Rep. Phys. Sci.*, vol. 2, no. 2, p. 100346, Feb. 2021, doi: 10.1016/j.xcrp.2021.100346.
[52] W. Shockley, “The theory of p-n junctions in semiconductors and p-n junction transistors,” *Bell Syst. Tech. J.*, vol. 28, no. 3, pp. 435–489, Jul. 1949, doi: 10.1002/j.1538-7305.1949.tb03645.x.
[53] J. Bang, S. Meng, and S. B. Zhang, “Dynamic defect as nonradiative recombination center in semiconductors,” *Phys. Rev. B*, vol. 100, no. 24, p. 245208, Dec. 2019, doi: 10.1103/PhysRevB.100.245208.
[54] O. Höhn, private communication, Apr. 23, 2025.
[55] J. Abdullayev and I. B. Sapaev, “Factors Influencing the Ideality Factor of Semiconductor p-n and p-i-n Junction Structures at Cryogenic Temperatures,” *East Eur. J. Phys.*, no. 4, Art. no. 4, Dec. 2024, doi: 10.26565/2312-4334-2024-4-37.
[56] CREE LED, “XLamp® XP-E2 LEDs.” Accessed: Nov. 01, 2024. [Online]. Available: https://downloads.cree-led.com/files/ds/x/XLamp-XPE2.pdf

[57] NREL, “Reference Air Mass 1.5 Spectra.” Accessed: Feb. 05, 2024. [Online]. Available: https://www.nrel.gov/grid/solar-resource/spectra-am1.5
[58] O. Er-Raji, private communication, Sep. 20, 2024.
[59] EPIGAP OSA, “OCI-490-20 ID980-XE-T Specifications.” Accessed: Nov. 01, 2024. [Online]. Available: https://www.epigap-osa.com/datasheet/OCI-490-20_ID980-XE.pdf
[60] O. Er-Raji, private communication, Apr. 09, 2025.
[61] S. C. Gillespie *et al.*, “Intensity-Modulated Photoluminescence Spectroscopy for Revealing Ionic Processes in Halide Perovskites,” *ACS Energy Lett.,* pp. 3122-3131, Jun. 2025, doi: 10.1021/acsenergylett.5c01102

Appendix A Extracted Current Densities per Wavelength for the Different Tandem Subcells from Illumination by LEDs and the Solar 1.5AM Spectrum

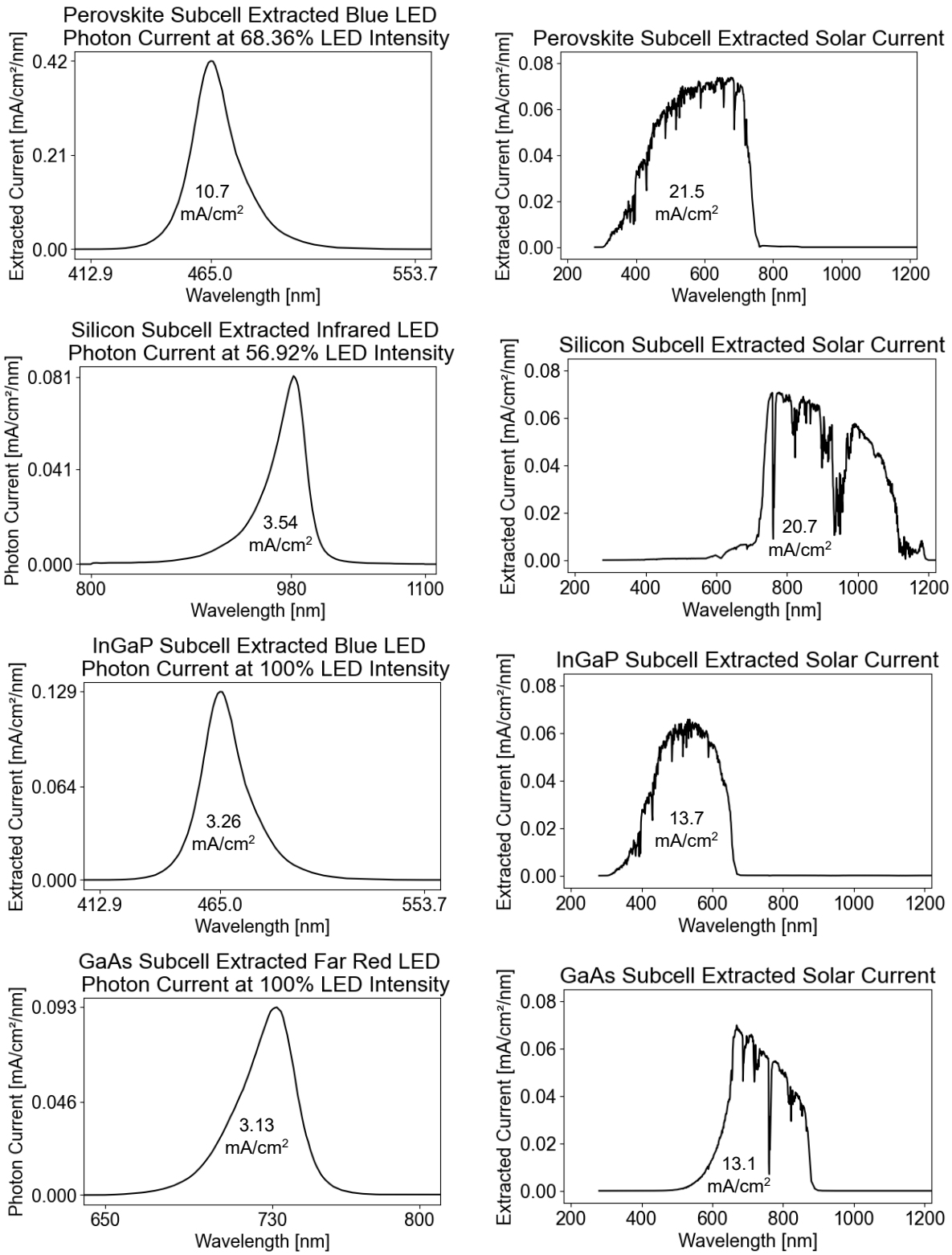

Figure 15. Extracted photogenetrated current densities per wavelength for the different tandem solar cell subcells from (left) the LEDs at specific Paios LED output intensities and (right) the solar spectrum. The calculations follow section 9.3. The top two rows correspond to the perovskite/silicon tandem solar cell's (first row) perovskite and (second row) silicon subcells. The EQEs used are from Fraunhofer ISE's measurements [58]. The bottom two rows correspond to the indium gallium phosphide/gallium arsenide tandem solar cell's (third row) indium gallium phosphide and (fourth row) gallium arsenide subcells. The EQEs used are from Fraunhofer ISE's measurements [54]. The LED spectra are derived from the data sheet for the blue and far-red LED [56] and the data sheet for the infrared LED [59]. The solar 1.5AM spectrum is taken from the NREL [57].

Appendix B Coupling Resistances to Model Inter-Subcell Recombination

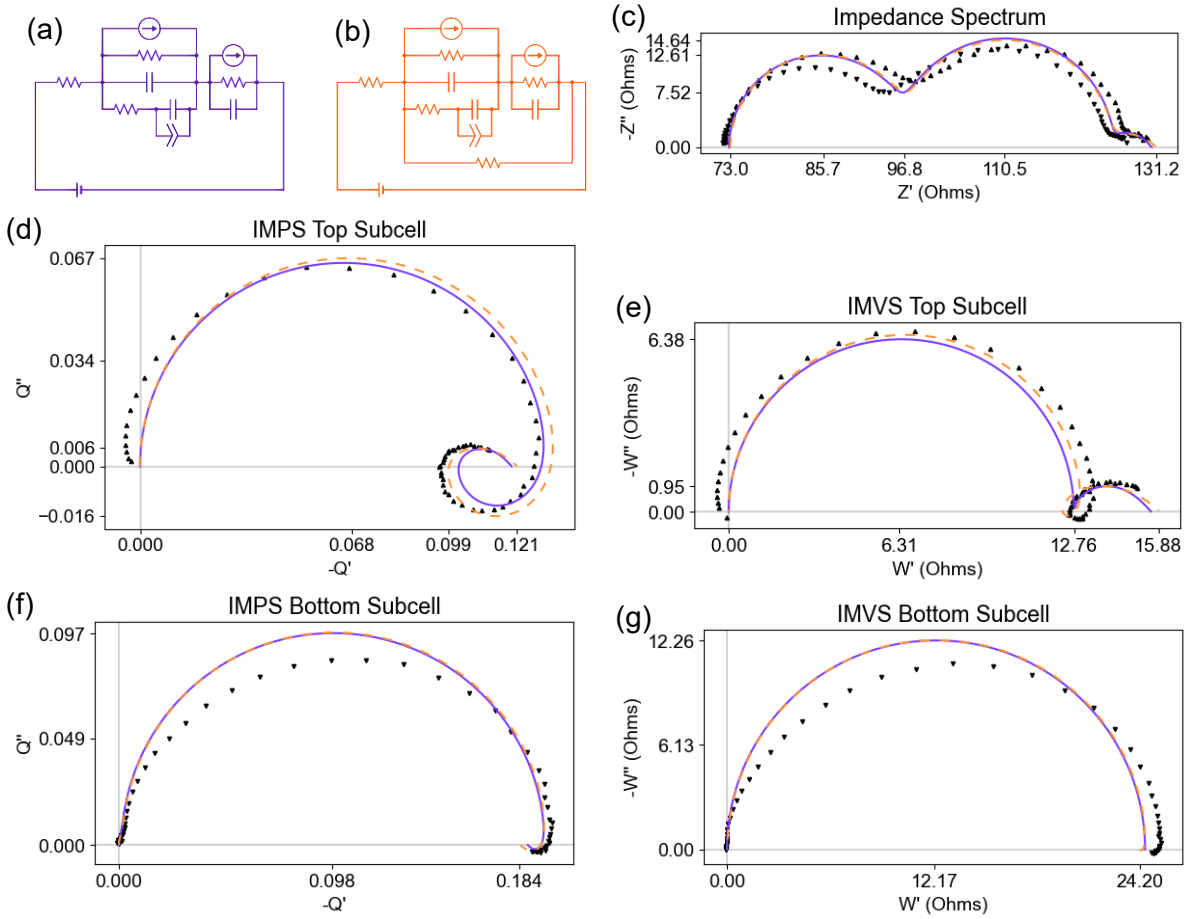

Figure 16. Comparison between a simplified equivalent circuit for a perovskite/silicon tandem solar cell (a) without and (b) with a coupling resistance used to simulate (c) the impedance spectrum, (d) the IMPS and (e) the IMVS response of the top subcell, as well as (f) the IMPS and (g) the IMVS response of the bottom subcell. The perovskite subcell was illuminated with the equivalent of 0.25 suns, whereas the silicon subcell was illuminated with the equivalent of 0.14 suns. The measured frequency range is 1 MHz – 1 Hz, and the fit curves have frequencies from 1 GHz to 1 mHz.

In the figure above, we observe a phenomenon where the IMVS graphs not only display the perturbed subcells but also negative features with the same characteristic frequencies as the non-perturbed subcells. This suggests that in these cases, there is some current also flowing through the non-perturbed subcells, allowing them to cause a response even when no current is extracted. One could assume that both subcells, therefore, are perturbed by the light modulation, though this would result in a positive response for both subcells in each IMVS spectrum. Thus, to model a negative response, a coupling resistance running parallel to the two subcells must be used.

As this element allows charges to recombine between the subcells without being extracted, a likely physical interpretation is that this coupling resistance models the recombination layer. A low resistance would imply that the electrons of the top subcell and the holes of the bottom subcell also recombine. A high coupling resistance, meanwhile, would suggest that only the top subcell's holes recombine with the bottom subcell's electrons, allowing the remaining (desired) charge carriers to be extracted.

Appendix C Equivalent-Circuit Parameter Values for the Silicon Photodiode

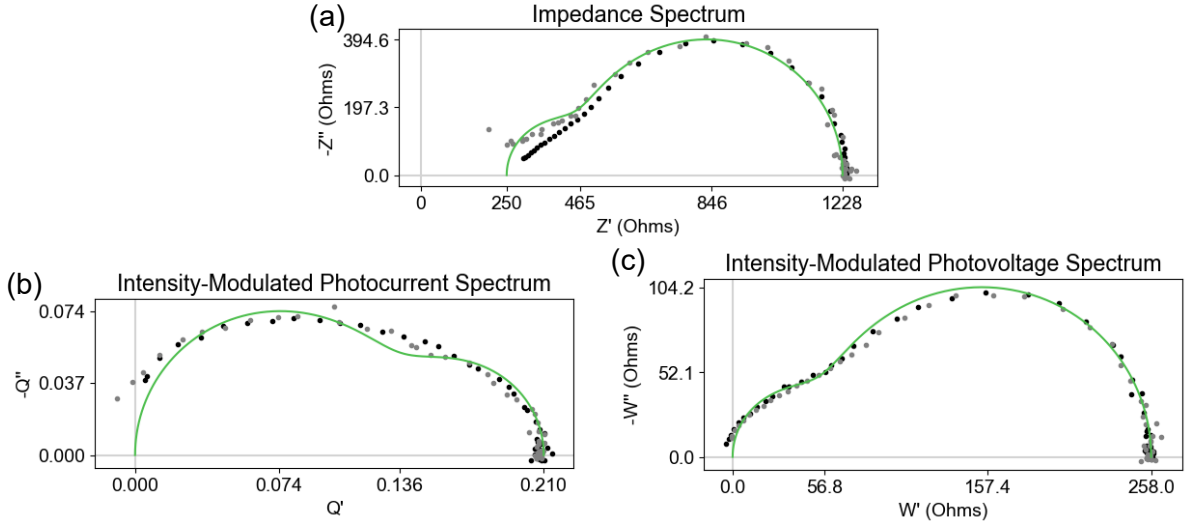

Figure 17. Results of fitting equivalent circuit 2a (see Figure 4) to the photodiode data from (a) impedance spectroscopy, (b) IMPS, and (c) IMVS. The measured frequency range is 1 MHz – 10 Hz, while the fit's upper limit is 1 GHz. The illumination is equivalent to 0.02 suns.

Table 3. Parameter results for the curve fits for the photodiode data in Figure 17. The characteristic times τ are found following [45]. The subscript "s" denotes series.The subscripts "1" and "2" refer to the low-frequency and high-frequency arcs, respectively. The subscripts "as" and "ext" relate to absorption-separation and extraction of charges, respectively. The errors are the standard deviations from the curve fits after being rounded up, with those for τ, EQE_{diff}, and η_{ext} found via error propagation, using $Eq.3$ for the former, and the equation for Q ($Eq.7$) with DC values for the latter two.

Parameter (units)	Value
$R_s\ (\Omega)$	250 ± 4
$R_s, corrected\ (\Omega)$	178 ± 4
$R_1\ (\Omega)$	215 ± 4
$C_1\ (nF)$	7.1 ± 0.4
$\tau_1\ (\mu s)$	1.53 ± 0.10
$R_2\ (\Omega)$	763 ± 6
$C_2\ (nF)$	32.8 ± 0.7
$\tau_2\ (\mu s)$	25.0 ± 0.6
$EQE_{diff}\ (\%)$	21.0 ± 0.3
$EQE_{diff}, corrected\ (\%)$	22.3 ± 0.3
$\eta_{as}\ (\%)$	26.4 ± 0.2
$\eta_{ext}\ (\%)$	79.6 ± 0.8
$\eta_{ext}, corrected\ (\%)$	84.6 ± 0.9

Appendix D Perovskite Solar Cell Simulations for IMPS and IMVS

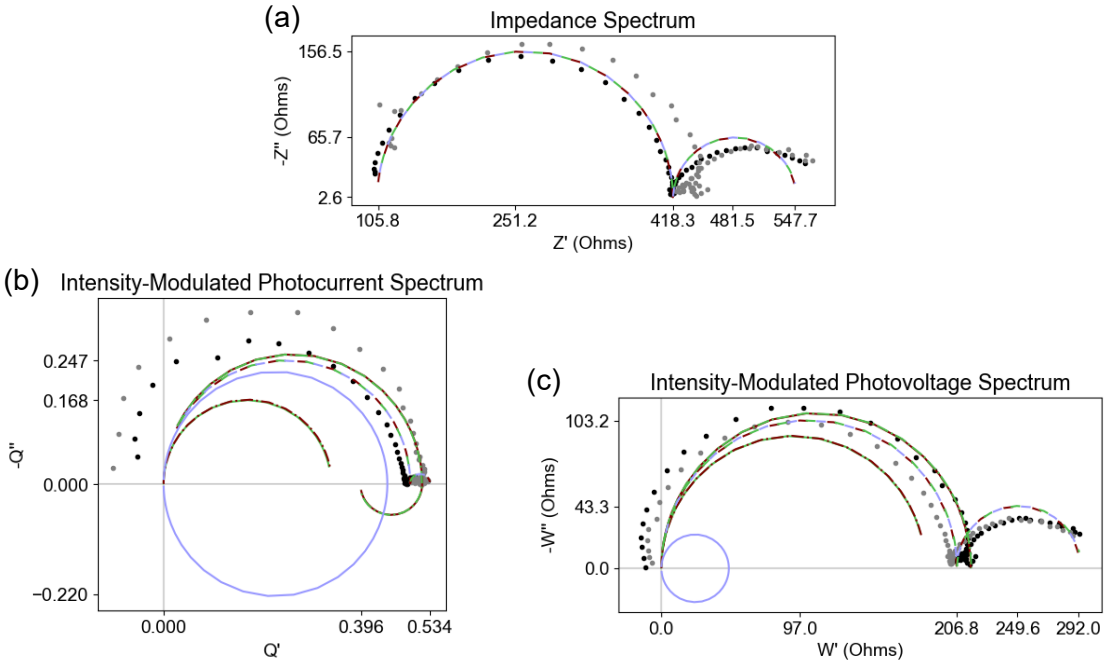

Figure 18. Simulations for all equivalent circuits in Figure 4 for the perovskite data from section 3.1.2.

Appendix E Example of Determining a Device's Absorption Efficiency

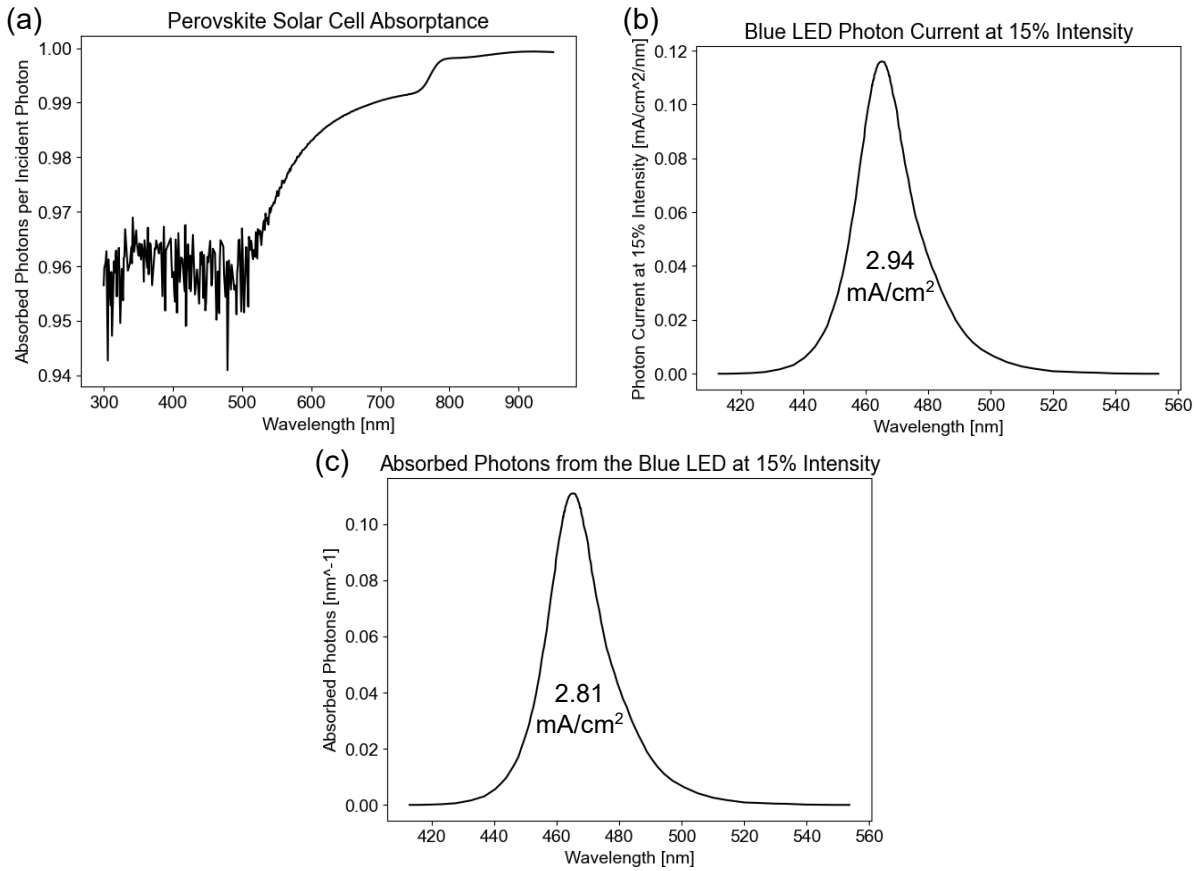

Figure 19. (a) The wavelength-resolved data for the perovskite sample in section 3.1.2 obtained by subtracting the reflectance data measured by our collaborators from Potsdam University [46] from 1. (b) The photon emission spectrum per wavelength of the LED is multiplied with the absorptance spectrum to find (c) the absorbed number of photons per wavelength. The ratio of the integrals (each integral value indicated under the respective graph) of the two latter spectra yields the absorption efficiency of the sample for the given light modulation.

Appendix F Simulations of Small-Perturbation Responses of the Perovskite Solar Cell Excluding Equipment Resistance

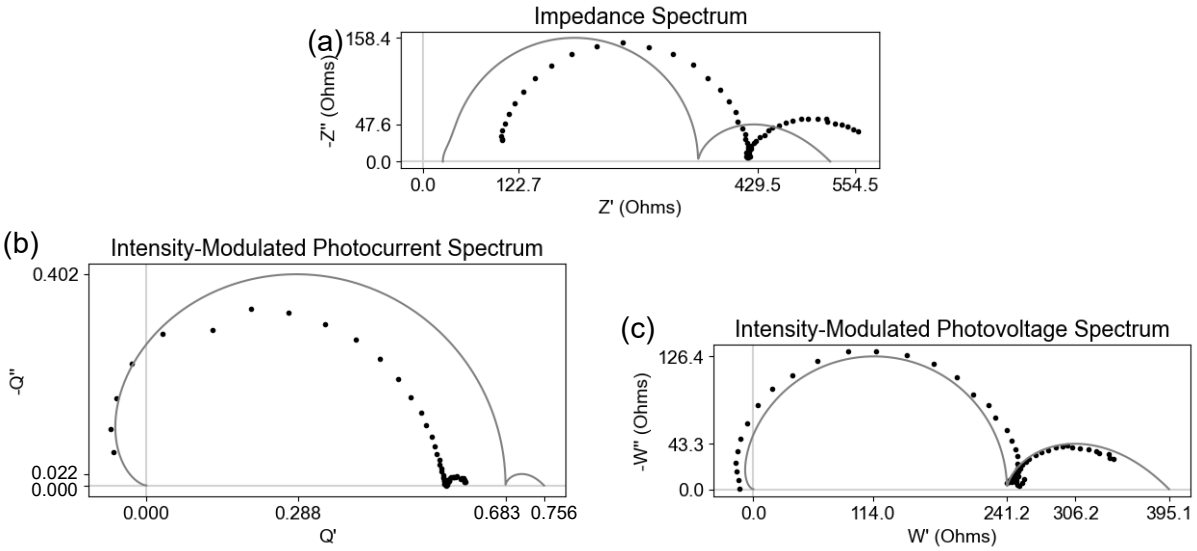

Figure 20. Simulated (a) impedance, (b) IMPS, and (c) IMVS responses for the perovskite data in Figure 4 when excluding the 72.1 Ω contribution to the series resistance caused by the measurement equipment.

Appendix G Curve-Fit Results from Measuring the III-V Tandem Solar Cell under 0.1 Sun-Equivalent Illumination and Partial Subcell Light-Flooding

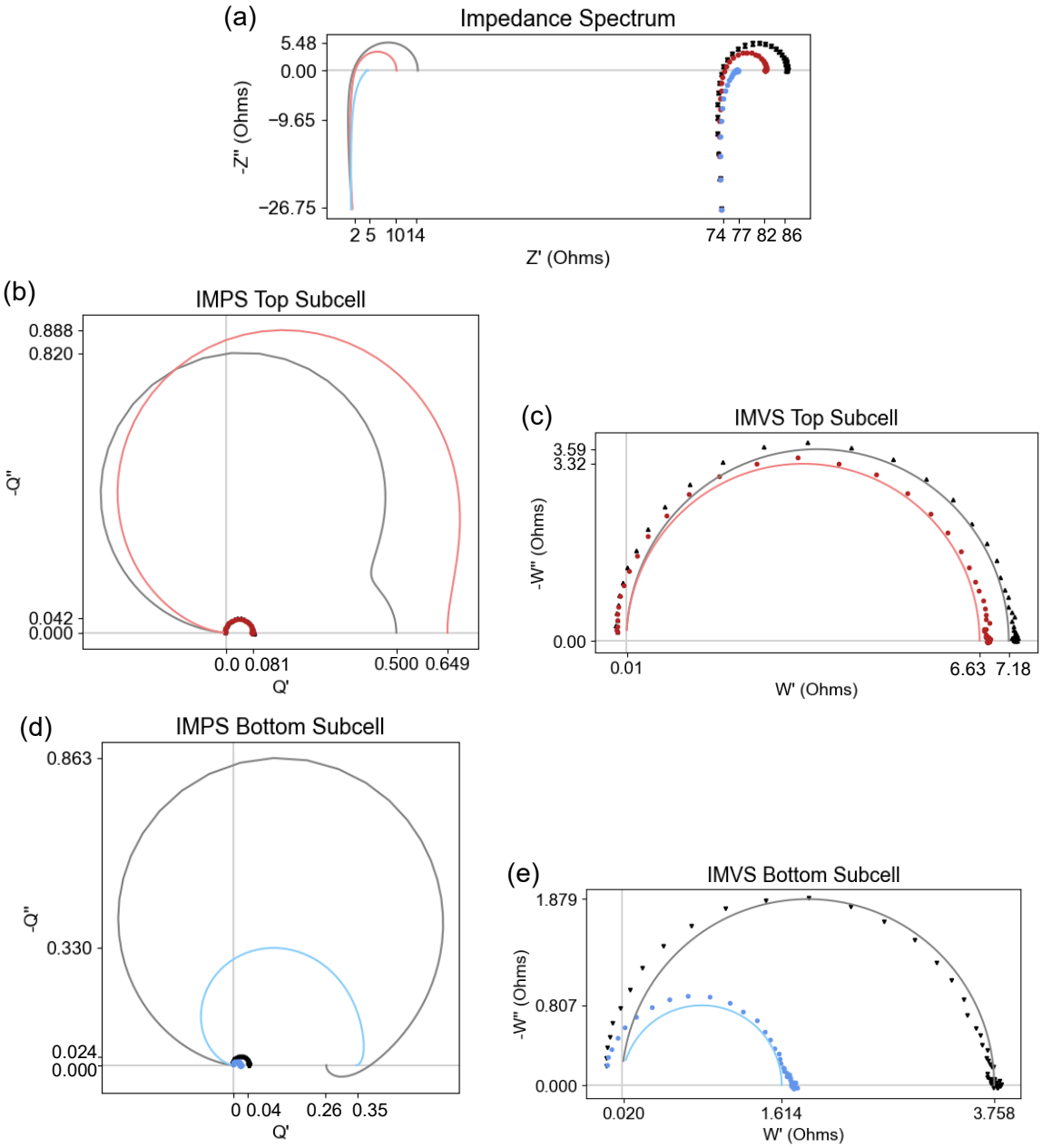

Figure 21. Simulations for (a) the impedance of the full III-V tandem solar cell, (b) the IMPS and (c) IMVS of the top subcell, as well as (d) the IMPS and (e) IMVS responses of the bottom subcell for different illumination conditions when excluding the internal resistance of 72.1 Ω of the measurement equipment from the series resistance. The measured data is the same as in Figure 6.

Table 4. Parameter fit values for the III-V tandem solar cell under different illumination conditions from Figures 6 and 21. The characteristic times τ are found following [45]. The subscript "s" denotes series.The subscripts "$InGaP$" and "$GaAs$" refer to the ingallium phosphide and gallium arsenide subcells, respectively. The subscript "rec" stands for recombination. The errors are the standard deviations from the curve fits after being rounded up, with those for τ, EQE_{diff}, and η_{ext} found via error propagation, using $Eq.3$ for the former, and the equation for Q $(Eq.7)$ with DC values for the latter two. The absorption efficiencies are obtained using the EQE spectra of the subcells measured by Fraunhofer ISE [54], which can be approximated to be equal to the absorptance [47], as well as the LED emission spectra, as shown in Appendix E. The corrected parameters are found using simulations of the system without the series resistance added by the measurement instrument.

Parameter (units)	Equal Illumination	GaAs Light-Flooded	InGaP Light-Flooded
R_s (Ω)	72.49 ± 0.05	72.7 ± 0.2	73.13 ± 0.06
R_s, corrected (Ω)	0.39 ± 0.05	0.6 ± 0.2	1.03 ± 0.06
R_{Con} $(k\Omega)$	0.68 ± 0.10	0.8 ± 0.2	3 ± 4
L_{Con} (μH)	4.364 ± 0.008	4.40 ± 0.03	4.404 ± 0.003
τ_{Con} (ns)	6.42 ± 0.02	5.50 ± 0.04	1.468 ± 0.002
R_{InGaP} (Ω)	8.0 ± 0.2	8.81 ± 0.06	0.350 ± 0.009
C_{InGaP} (μF)	0.67 ± 0.02	0.595 ± 0.006	53 ± 3
τ_{InGaP} (μs)	5.4 ± 0.3	5.24 ± 0.07	19 ± 2
R_{GaAs} (Ω)	6.0 ± 0.2	0.8 ± 0.2	3.29 ± 0.02
C_{GaAs} (μF)	0.408 ± 0.009	0.5 ± 0.2	0.297 ± 0.003
τ_{GaAs} (μs)	2.45 ± 0.10	0.4 ± 0.2	0.98 ± 0.02
$EQE_{InGaP,diff}$ (%)	8.3 ± 0.3	8.06 ± 0.09	N/A
$EQE_{InGaP,diff}$, corrected (%)	50 ± 2	65 ± 2	N/A
$\eta_{InGaP,abs}$ (%)	95.0	95.0	95.0
$\eta_{InGaP,sep}$ (%)	95 ± 2	79.3 ± 0.6	N/A
$\eta_{InGaP,ext}$ (%)	9.2 ± 0.3	10.70 ± 0.09	N/A
$\eta_{InGaP,ext}$, corrected (%)	56 ± 2	86 ± 3	N/A
$EQE_{GaAs,diff}$ (%)	4.3 ± 0.3	N/A	2.11 ± 0.02
$EQE_{GaAs,diff}$, corrected (%)	26 ± 2	N/A	34.5 ± 0.6
$\eta_{GaAs,abs}$ (%)	84.0	84.0	84.0
$\eta_{GaAs,sep}$ (%)	75 ± 2	N/A	58.4 ± 0.06
$\eta_{GaAs,ext}$ (%)	6.9 ± 0.3	N/A	4.31 ± 0.03
$\eta_{GaAs,ext}$, corrected (%)	42 ± 2	N/A	71 ± 2

Appendix H Current-Voltage Curves of the III-V Tandem Solar Cell under 0.1 Sun-Equivalent Illumination and Partial Subcell Light-Flooding

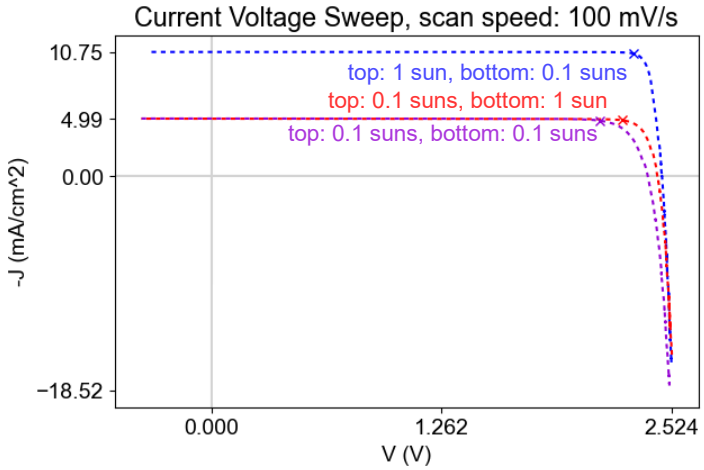

Figure 22. Current-voltage measurements of the InGaP/GaAs tandem solar cell under different equivalent-illumination conditions.

Appendix I Measured and Reconstructed Small-Perturbation Responses of the III-V Tandem Solar Cell

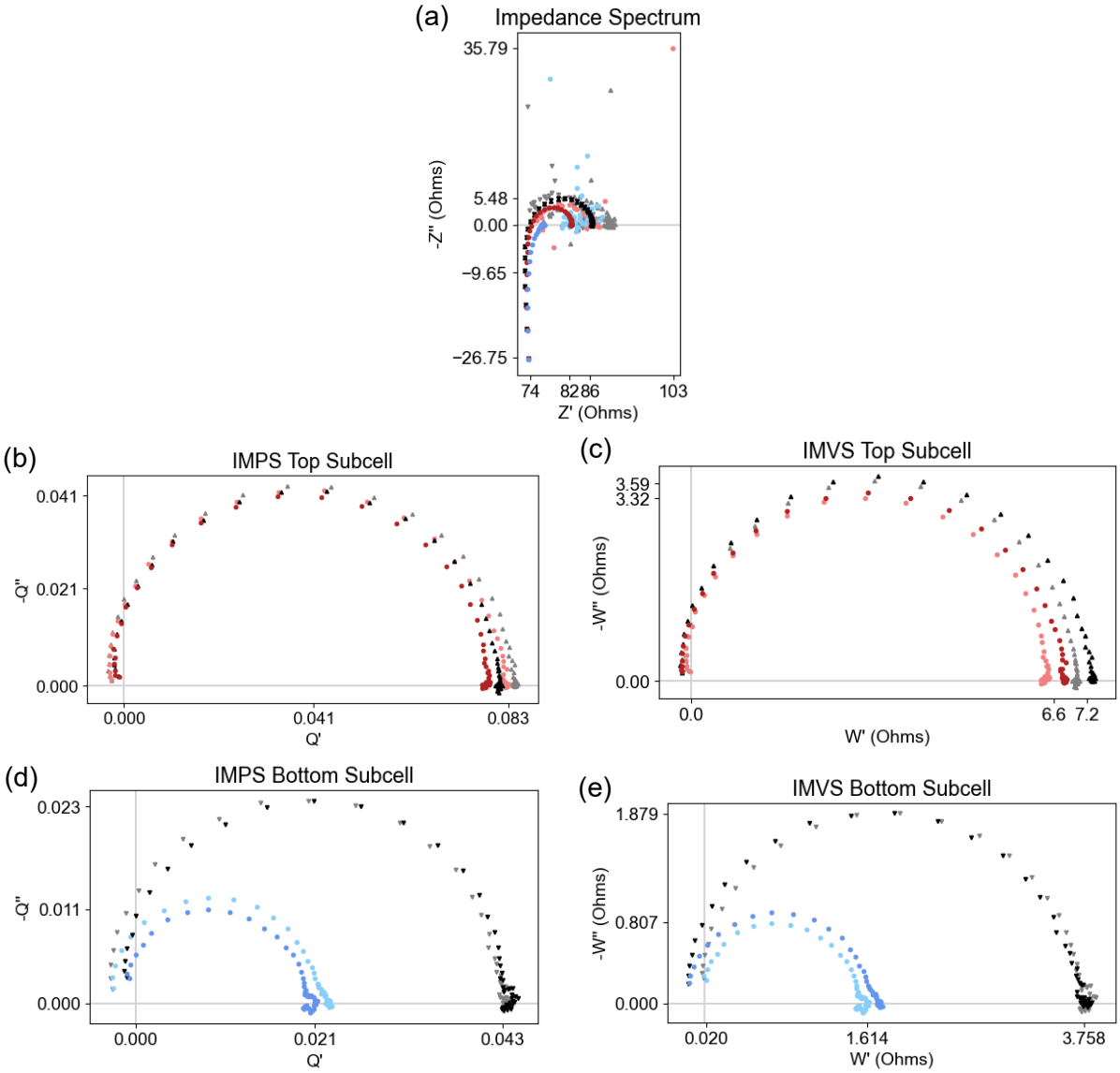

Figure 23. Data for (a) the impedance of the full III-V tandem solar cell, (b) the IMPS and (c) IMVS of the top subcell, as well as (d) the IMPS and (e) IMVS responses of the bottom subcell for different illumination conditions when excluding the internal resistance of 72.1 Ω of the measurement equipment from the series resistance. The saturated points correspond to the measured data in Figure 6, whereas the paler points correspond to the data reconstructed by calculating the response based on the other two measurements.

Appendix J Modeling the III-V Tandem Solar Cells with Added Transport Resistance-Capacitance Pairs

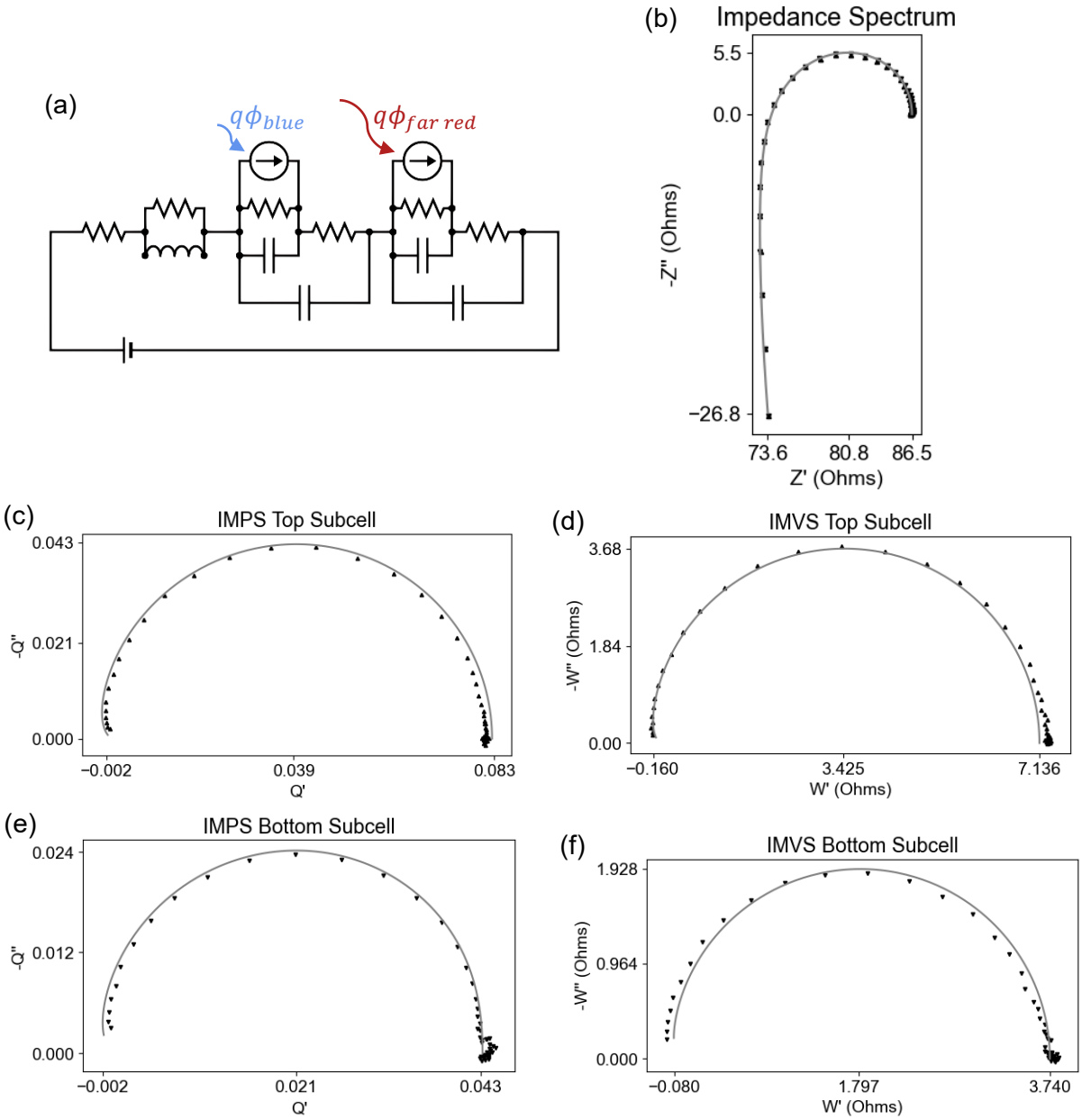

Figure 24. (a) The equivalent circuit, including recombination and transport resistance-capacitance pairs for both subcells used to fit (b) the impedance of the III-V tandem solar cell, (c) the top subcell's IMPS and (d) IMVS data, and (e) the bottom subcell's IMPS and (f) IMVS data at open-circuit voltage. The measured data corresponds to the equal-illumination data in Figure 6.

Table 5. Parameter values for the curve fits of the III-V tandem solar cell in Figure 24, considering recombination and transport processes for each subcell. The characteristic times τ are found following [45]. The subscript "s" denotes series. The subscripts "$InGaP$" and "$GaAs$" refer to the indium gallium phosphide and gallium arsenide subcells, respectively. The subscript "rec" stands for recombination, while "tra" means transport. The errors are the standard deviations from the curve fits after being rounded up, with those for τ, EQE_{diff}, and η_{ext} found via error propagation, using $Eq.3$ for the former, and the equation for Q $(Eq.7)$ with DC values for the latter two. The absorption efficiencies are obtained using the EQE spectra of the subcells measured by Fraunhofer ISE [54], which can be approximated to be equal to the absorptance [47], as well as the LED emission spectra, as shown in Appendix E. The corrected parameters are found using simulations of the system without the series resistance added by the measurement instrument.

Parameter (units)	Value
R_s (Ω)	72.10 ± 0.09
R_s, corrected (Ω)	0.00 ± 0.09
R_{Con} $(k\Omega)$	0.63 ± 0.07
L_{Con} (μH)	4.40 ± 0.01
τ_{Con} (ns)	6.98 ± 0.02
$R_{InGaP,rec}$ (Ω)	7.91 ± 0.02
$C_{InGaP,rec}$ (μF)	0.37 ± 0.03
$\tau_{InGaP,rec}$ (ms)	2.9 ± 0.3
$R_{InGaP,tra}$ (Ω)	1.12 ± 0.10
$C_{InGaP,tra}$ (μF)	0.27 ± 0.02
$\tau_{InGaP,tra}$ (μs)	0.30 ± 0.04
$R_{GaAs,rec}$ (Ω)	4.69 ± 0.02
$C_{GaAs,rec}$ (μF)	0.22 ± 0.03
$\tau_{GaAs,rec}$ (μs)	1.0 ± 0.2
$R_{GaAs,tra}$ (Ω)	0.66 ± 0.05
$C_{GaAs,tra}$ (μF)	0.27 ± 0.03
$\tau_{GaAs,tra}$ (μs)	0.18 ± 0.03
$EQE_{InGaP,diff}$ (%)	8 ± 3
$EQE_{InGaP,diff}$, corrected (%)	50 ± 20
$\eta_{InGaP,abs}$ (%)	95.0
$\eta_{InGaP,sep}$ (%)	100 ± 30
$\eta_{InGaP,ext}$ (%)	9.14 ± 0.03
$\eta_{InGaP,ext}$, corrected (%)	55.0 ± 0.6
$EQE_{GaAs,diff}$ (%)	4 ± 4
$EQE_{GaAs,diff}$, corrected (%)	30 ± 30
$\eta_{GaAs,abs}$ (%)	84.0
$\eta_{GaAs,sep}$ (%)	100 ± 70
$\eta_{GaAs,ext}$ (%)	5.42 ± 0.03
$\eta_{GaAs,ext}$, corrected (%)	32.6 ± 0.4

Appendix K Measured and Reconstructed Small-Perturbation Responses of the Degraded Perovskite/Silicon Tandem Solar Cell

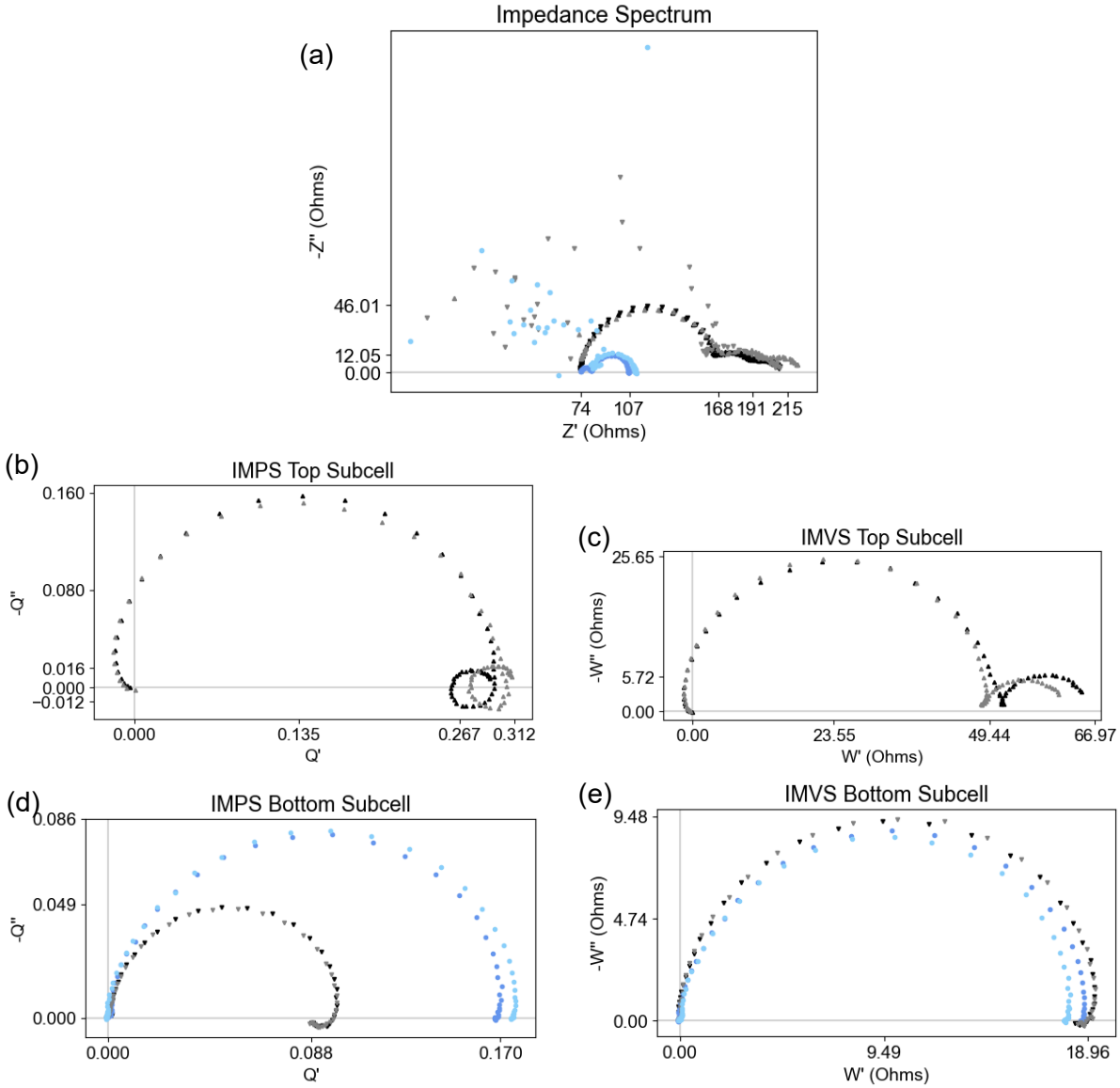

Figure 25. Data for (a) the impedance of the full, degraded perovskite/silicon tandem solar cell, (b) the IMPS and (c) IMVS of the top subcell, as well as (d) the IMPS and (e) IMVS responses of the bottom subcell for different illumination conditions. The saturated points correspond to the measured data in Figures 8 and 9, whereas the paler points correspond to the data reconstructed by calculating the response based on the other two measurements.

Appendix L Parameter Values of the Degraded Perovskite/Silicon Tandem Solar Cell under Equal Illumination and under Light-Flooding of the Perovskite

Table 6. Parameter values for curve fits of the perovskite/silicon tandem solar cell under different illumination conditions in Figures 8 and 9. The characteristic times τ are found following [45]. The subscript "s" denotes series.The subscripts "Pvk" and "Si" refer to the perovskite and silicon subcells, respectively. The subscript "rec" stands for recombination, with the following abbreviations "ele" and "ion" describing the nature of the recombination as electronic and ionic, respectively. The subscript "tra" means transport. The errors are the standard deviations from the curve fits after being rounded up, with those for τ, EQE_{diff}, and η_{ext} found via error propagation, using $Eq.3$ for the former, and the equation for Q $(Eq.7)$ with DC values for the latter two. The values for the absorption efficiency are based on the absorption spectra of the subcells as calculated by Fraunhofer ISE [60] and the LED spectra, following the method in Appendix E. The corrected parameters are found using simulations of the system without the series resistance added by the measurement instrument.

Parameter (units)	Equal Illumination	Perovskite Light-Flooded
R_s (Ω)	73.7 ± 0.4	73.6 ± 0.2
R_s, corrected (Ω)	1.6 ± 0.4	1.5 ± 0.2
$R_{Pvk,rec,ele}$ (Ω)	102 ± 1	6 ± 3
$C_{Pvk,rec,ele}$ (μF)	0.049 ± 0.005	0.4 ± 0.7
$\tau_{Pvk,rec,ele}$ (μs)	5.0 ± 0.6	2 ± 5
$R_{Pvk,rec,ion}$ (Ω)	300 ± 7	3 ± 4
$C_{Pvk,rec,ion}$ (μF)	31 ± 2	20 ± 20
CPE_{Pvk} $(mF * s^{-0.5})$	0.21 ± 0.02	2 ± 2
$\tau_{Pvk,rec,ion}$ (ms)	13.3 ± 0.9	0.1 ± 0.2
$R_{Pvk,tra}$ (Ω)	16.1 ± 0.9	6 ± 2
$C_{Pvk,tra}$ (μF)	0.081 ± 0.005	0.16 ± 0.03
$\tau_{Pvk,tra}$ (μs)	1.3 ± 0.2	1.0 ± 0.4
$R_{Si,rec,ele}$ (Ω)	23.8 ± 0.3	21.9 ± 1.0
$C_{Si,rec,ele}$ (μF)	25.5 ± 0.3	26 ± 2
$\tau_{Si,rec,ele}$ (ms)	0.61 ± 0.02	0.57 ± 0.06
$EQE_{Pvk,diff}$ (%)	30.7 ± 0.6	N/A
$EQE_{Pvk,diff}$, corrected (%)	46.2 ± 1.0	N/A
$\eta_{Pvk,abs}$ (%)	88.6	N/A
$\eta_{Pvk,sep}$ (%)	73.5 ± 0.9	N/A
$\eta_{Pvk,ext}$ (%)	47.2 ± 0.6	N/A
$\eta_{Pvk,ext}$, corrected (%)	71.0 ± 1.0	N/A
$EQE_{Si,diff}$ (%)	8.8 ± 0.2	17 ± 2
$EQE_{Si,diff}$, corrected (%)	13.2 ± 0.3	51 ± 7
$\eta_{Si,abs}$ (%)	95.1	85.1
$\eta_{Si,sep}$ (%)	83.8 ± 0.1	87 ± 4
$\eta_{Si,ext}$ (%)	11.0 ± 0.2	20 ± 2
$\eta_{Si,ext}$, corrected (%)	16.6 ± 0.3	62 ± 8

Appendix M Small-Perturbation Data and Parameter Values of the Less-Degraded Perovskite/Silicon Tandem Solar Cell under Light-Flooding of the Silicon and under Equal Illumination

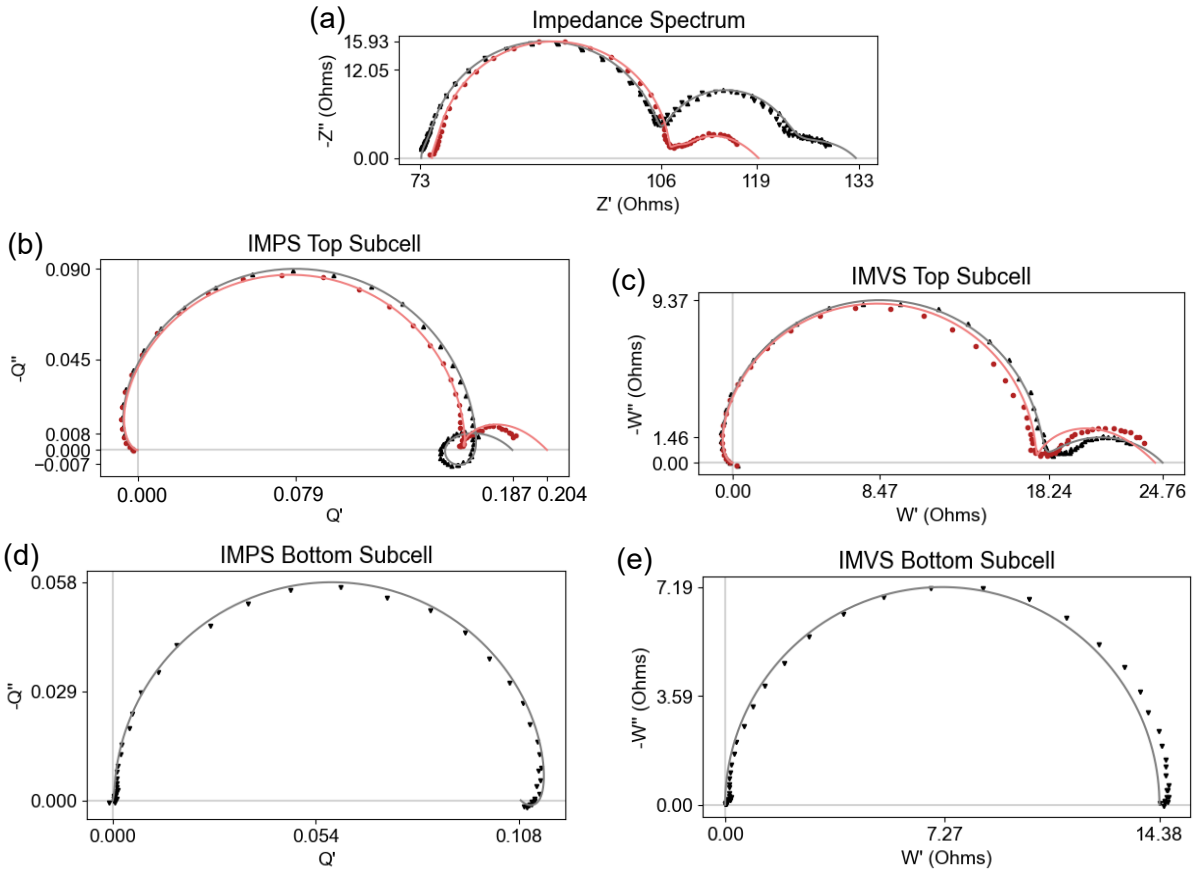

Figure 26. Comparison of data of (a) the impedance spectrum of the less-degraded perovskite/silicon tandem solar cell, (b) its IMPS and (c) IMVS responses when light-perturbing the perovskite subcell, and (d) its IMPS and (e) IMVS responses when light-perturbing the silicon subcell. Under equal illumination, both subcells generate the same amount of photocurrent as under 0.1 sun illumination. In contrast, when flooded, the top subcell generates the same amount of photocurrent as under 1 sun. The frequency range is 1 MHz – 1 Hz.

Table 7. Parameter values for the curve fits of the perovskite/silicon tandem solar cell under different illumination conditions shown in Figure 26. The characteristic times τ are found following [45]. The subscript "s" denotes series.The subscripts "Pvk" and "Si" refer to the perovskite and silicon subcells, respectively. The subscript "rec" stands for recombination, with the following abbreviations "ele" and "ion" describing the nature of the recombination as electronic and ionic, respectively. The subscript "tra" means transport. The errors are the standard deviations from the curve fits after being rounded up, with those for τ, EQE_{diff}, and η_{ext} found via error propagation, using $Eq.3$ for the former, and the equation for Q $(Eq.7)$ with DC values for the latter two. The values for the absorption efficiency are based on the absorption spectra of the subcells as calculated by Fraunhofer ISE [60] and the LED spectra, following the method in Appendix E. The corrected parameters are found using simulations of the system without the series resistance added by the measurement instrument.

Parameter (units)	Equal Illumination	Silicon Light-Flooded
R_s (Ω)	73.2 ± 0.2	74.6 ± 0.2
R_s, corrected (Ω)	1.1 ± 0.2	2.5 ± 0.2
$R_{Pvk,rec,ele}$ (Ω)	36.5 ± 0.4	36.1 ± 0.7
$C_{Pvk,rec,ele}$ (μF)	0.119 ± 0.006	0.102 ± 0.010
$\tau_{Pvk,rec,ele}$ (μs)	4.3 ± 0.3	3.7 ± 0.4
$R_{Pvk,rec,ion}$ (Ω)	94 ± 2	92 ± 3
$C_{Pvk,rec,ion}$ (μF)	9 ± 6	101 ± 7
CPE_{Pvk} $(mF * s^{-0.5})$	1.97 ± 0.09	1.11 ± 0.08
$\tau_{Pvk,rec,ion}$ (ms)	35 ± 3	20 ± 2
$R_{Pvk,tra}$ (Ω)	6.3 ± 3	6.6 ± 0.5
$C_{Pvk,tra}$ (μF)	0.133 ± 0.006	0.154 ± 0.009
$\tau_{Pvk,tra}$ (μs)	0.8 ± 0.5	1.02 ± 0.10
$R_{Si,rec,ele}$ (Ω)	16.6 ± 0.2	2.0 ± 0.2
$C_{Si,rec,ele}$ (μF)	52.1 ± 0.4	480 ± 70
$\tau_{Si,rec,ele}$ (ms)	0.86 ± 0.02	1.0 ± 0.2
$EQE_{Pvk,diff}$ (%)	18.7 ± 0.6	20.4 ± 0.8
$EQE_{Pvk,diff}$, corrected (%)	41 ± 3	52 ± 3
$\eta_{Pvk,abs}$ (%)	88.6	88.6
$\eta_{Pvk,sep}$ (%)	76.6 ± 0.8	76 ± 2
$\eta_{Pvk,ext}$ (%)	27.5 ± 2	30.2 ± 0.7
$\eta_{Pvk,ext}$, corrected (%)	60 ± 4	77 ± 3
$EQE_{Si,diff}$ (%)	10.9 ± 0.3	N/A
$EQE_{Si,diff}$, corrected (%)	24 ± 2	N/A
$\eta_{Si,abs}$ (%)	95.1	N/A
$\eta_{Si,sep}$ (%)	91.1 ± 0.6	N/A
$\eta_{Si,ext}$ (%)	12.5 ± 0.4	N/A
$\eta_{Si,ext}$, corrected (%)	27 ± 2	N/A

Appendix N Simulations of Small-Perturbation Responses of the Perovskite/Silicon Tandem Solar Cell Before and After Degradation Excluding Equipment Resistance

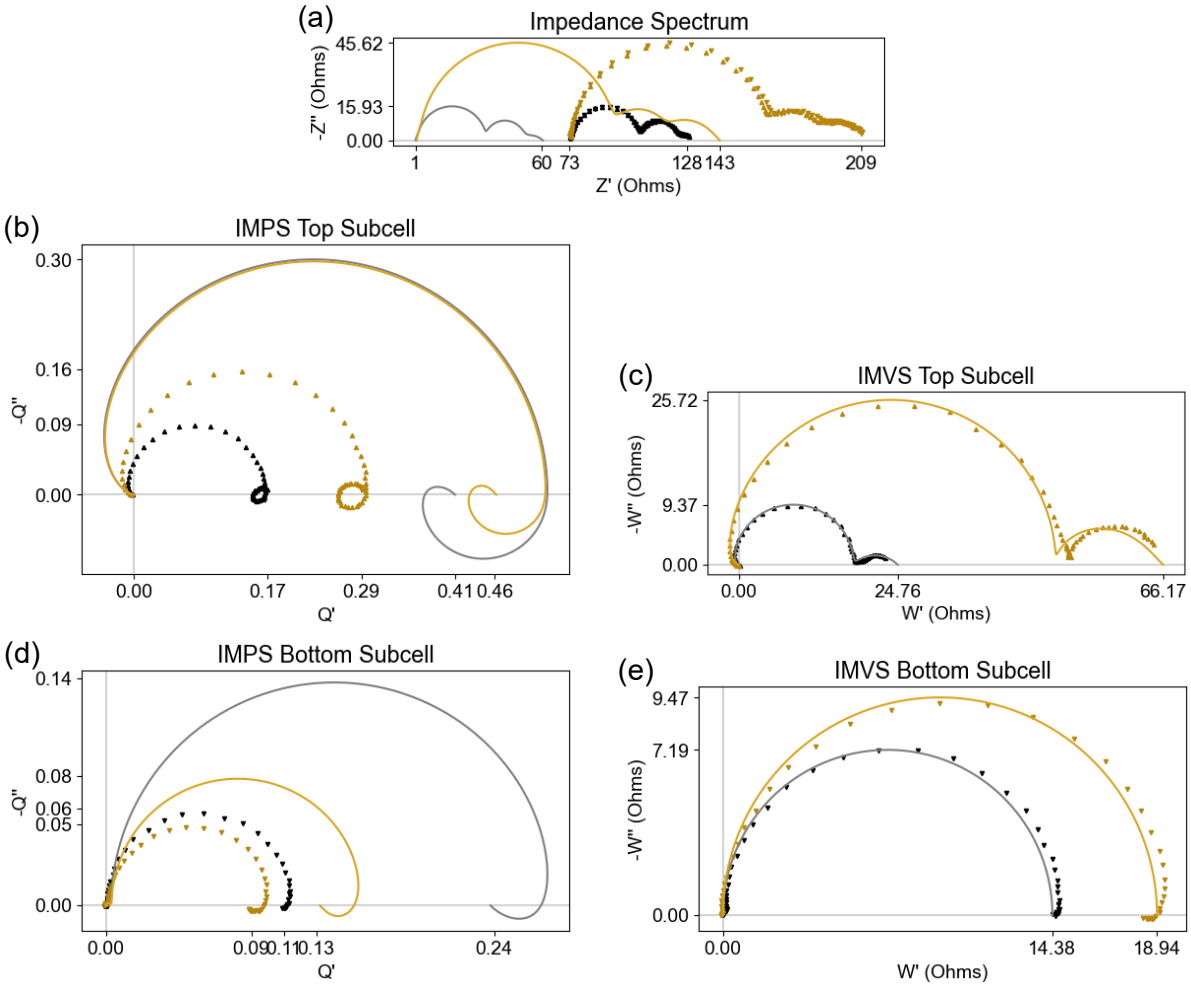

Figure 27. Simulations for (a) the impedance of the (more and less degraded) perovskite/silicon tandem solar cell, (b) the IMPS and (c) IMVS of the top subcell, as well as (d) the IMPS and (e) IMVS responses of the bottom subcell when excluding the internal resistance of 72.1 Ω of the measurement equipment from the series resistance. The measured data is the same as in Figure 10.

Appendix O Current-Voltage Responses of the Perovskite/Silicon Tandem Solar Cell under 0.1 Suns Before and After Degradation

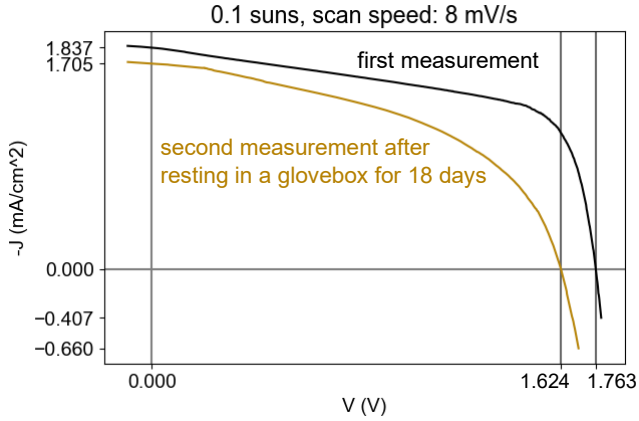

Figure 28. Current-voltage response of the perovskite/silicon solar cell before and after storage in a dark, nitrogen-filled glovebox for 18 days.

Appendix P Parameter Results of the Intensity-Modulated Measurements on the Silicon Photodiode at Various Offset Light Intensities

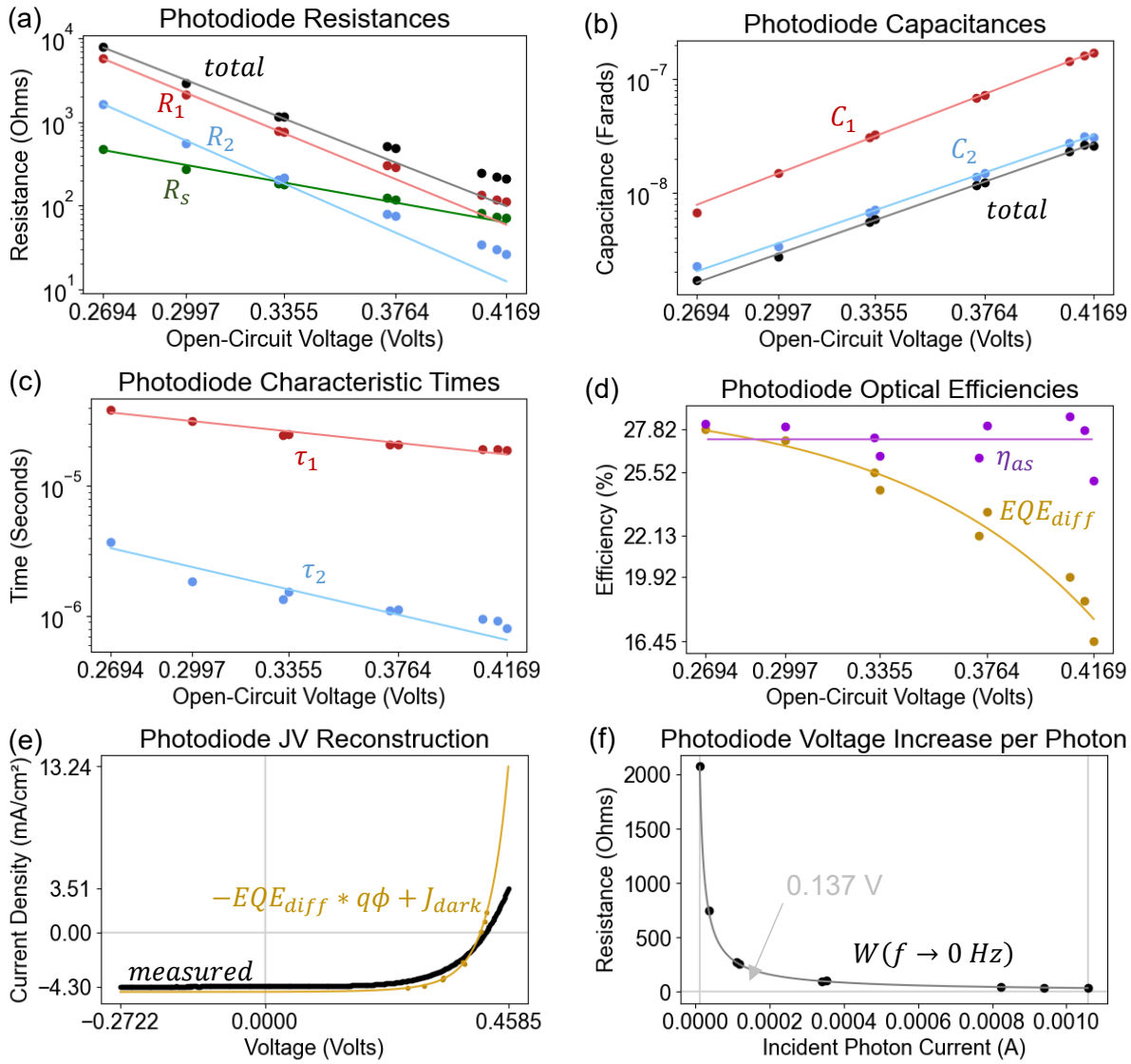

Figure 29. Results from measuring the small-perturbation techniques on the silicon photodiode at different offset illuminations. Subfigures (a-d) display the parameter fits for the resistances, capacitances, characteristic times, and optical efficiencies for the LED used, respectively. Subfigure (e) compares a measured current-voltage response with a reconstruction following the steps in section 6.1.1 using the ideality factor and $R(\bar{V}_{app} = 0\ V)$ from the resistance trends for the dark current and the incoming photon current multiplied by $-EQE_{diff}$ for the photogenerated current. Subfigure (f) maps the dependence of $W(f \to 0\ Hz)$ on the incoming photocurrent to find the added photovoltage from changing illumination by taking the integral between the two values of $W(q\phi, f \to 0\ Hz)$.

Appendix Q Parameter Results of the Intensity-Modulated Measurements on the Perovskite Solar Cell at Various Offset Light Intensities

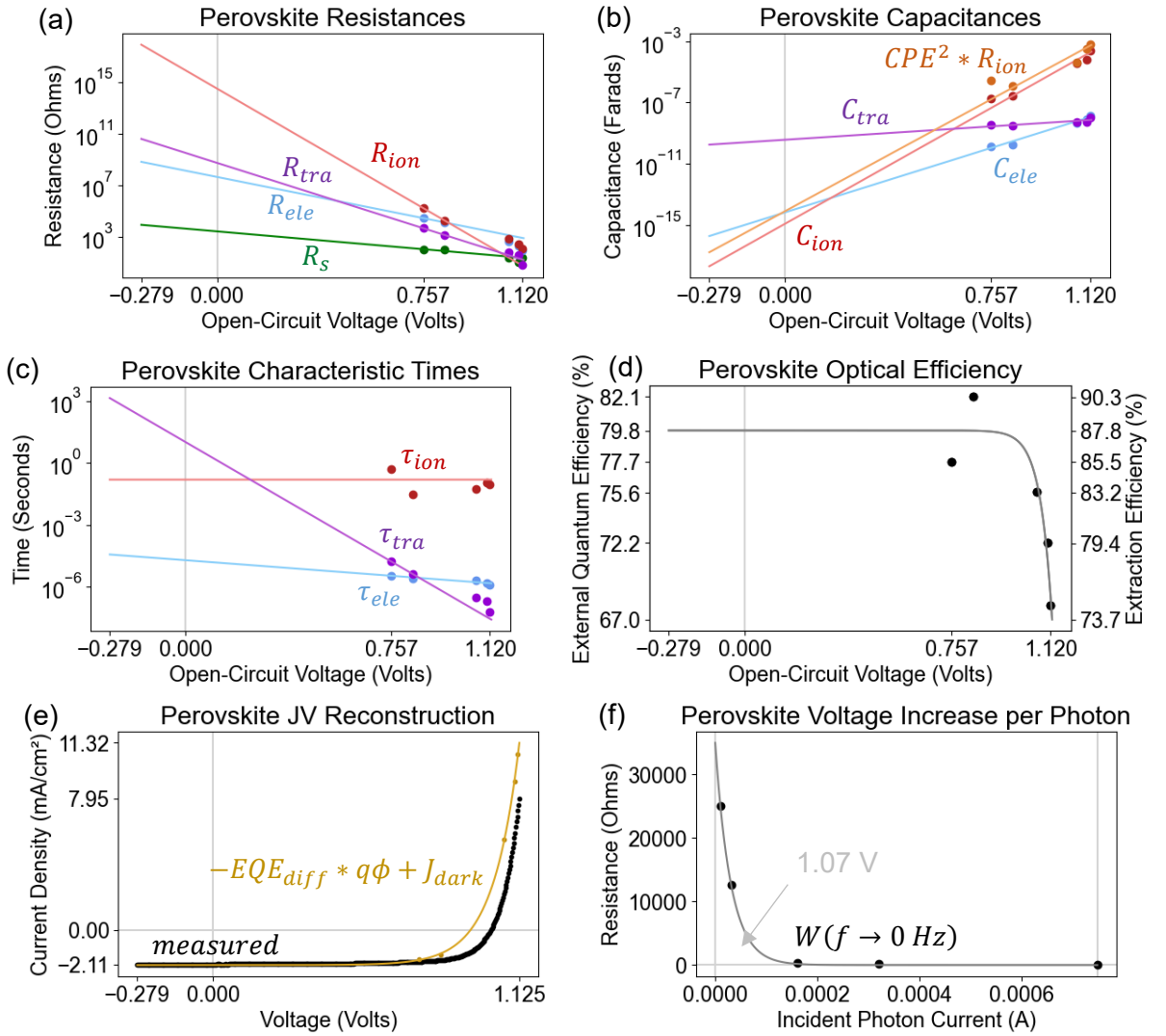

Figure 30. Results from measuring the small-perturbation techniques on the perovskite solar cell at different offset illuminations. Subfigures (a-d) display the parameter fits for the resistances, capacitances, characteristic times, and optical efficiencies for the LED used, respectively. Subfigure (e) compares a measured current-voltage response with a reconstruction following the steps in section 6.1.1 using the ideality factor and $R(\bar{V}_{app} = 0\ V)$ from the resistance trends for the dark current and the incoming photon current multiplied by $-EQE_{diff}$ for the photogenerated current. Subfigure (f) maps the dependence of $W(f \rightarrow 0\ Hz)$ on the incoming photocurrent to find the added photovoltage from changing illumination by taking the integral between the two values of $W(q\phi, f \rightarrow 0\ Hz)$.

Appendix R Additional Parameter Results of the Intensity-Modulated Measurements on the InGaP/GaAs Tandem Solar Cell at Various Offset Light Intensities

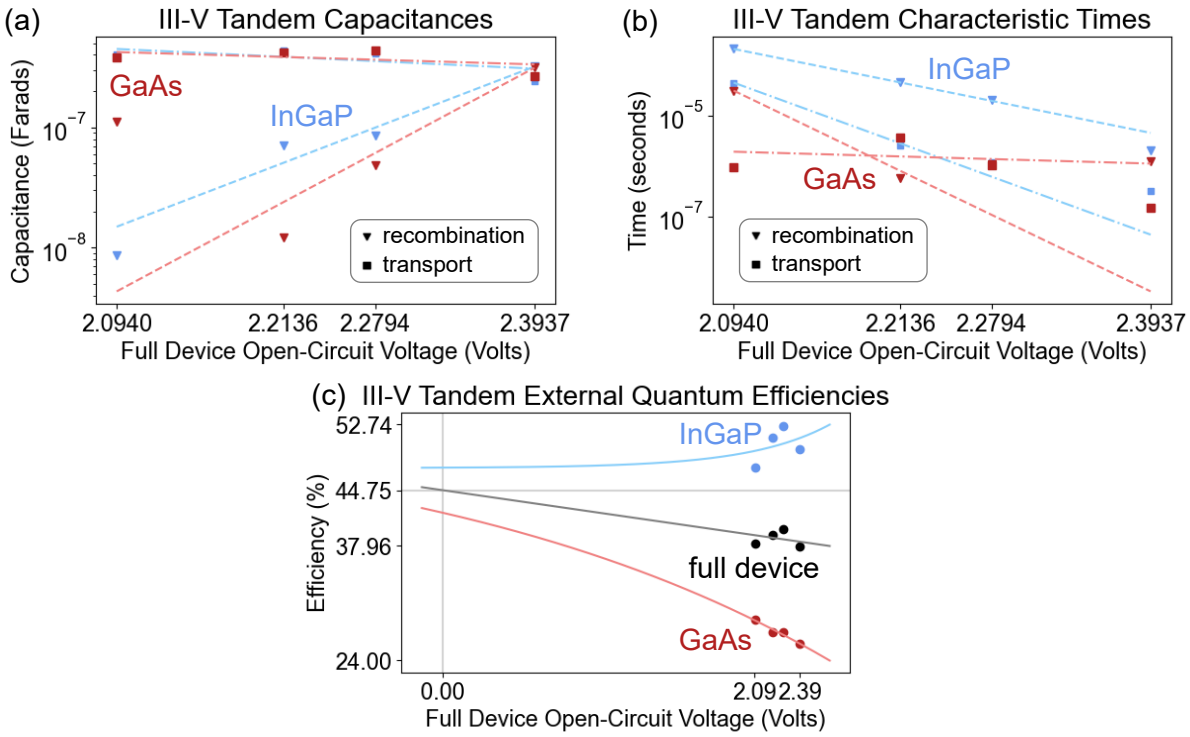

Figure 31. Illumination-dependent parameter trends for (a) the capacitances, (b) characteristic times, and (c) external quantum efficiencies of the III-V tandem solar cells for the LEDs used. The extraction efficiencies at 0 V are assumed to be 50%, with the full-device extraction and external quantum efficiencies assumed to be the average of the subcell extraction and external quantum efficiencies.

Appendix S Additional Parameter Results of the Intensity-Modulated Measurements on the Perovskite/Silicon Tandem Solar Cell at Various Offset Light Intensities

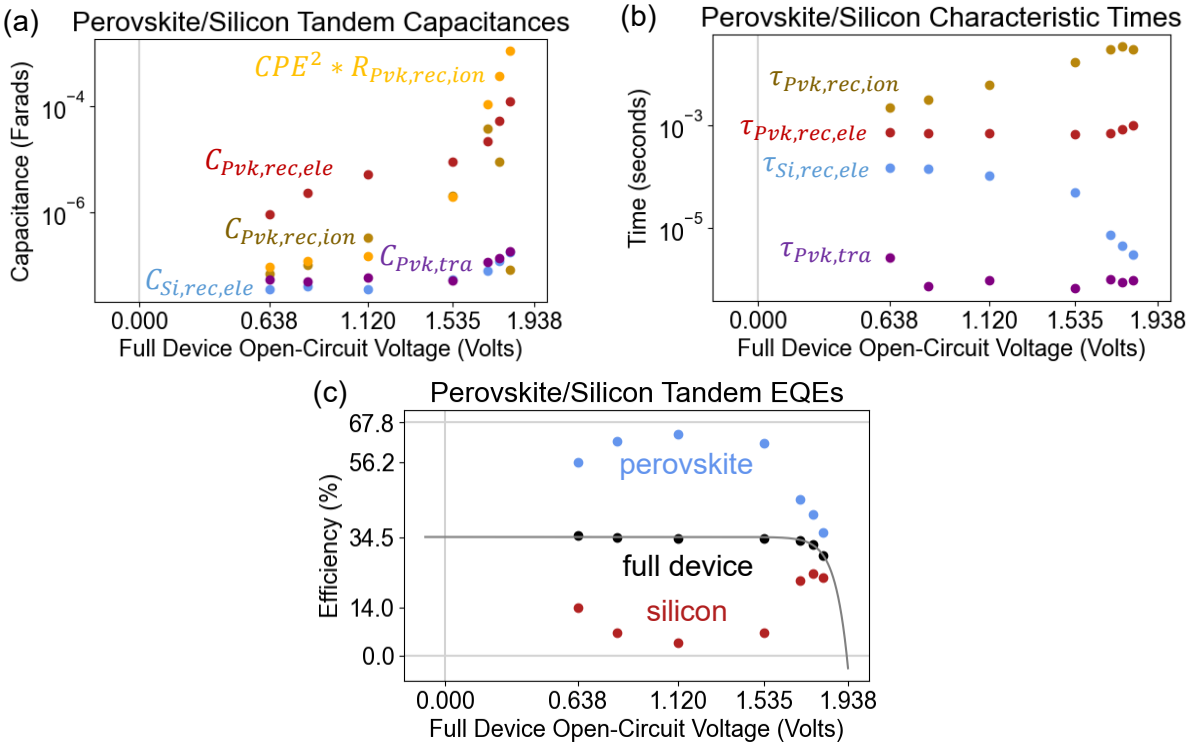

Figure 32. Illumination-dependent parameter trends for (a) the capacitances, (b) characteristic times, and (c) external quantum efficiencies of the perovskite/silicon tandem solar cells for the LEDs used.

Appendix T Examples of Raw Data Constituting the Small-Perturbation Spectra

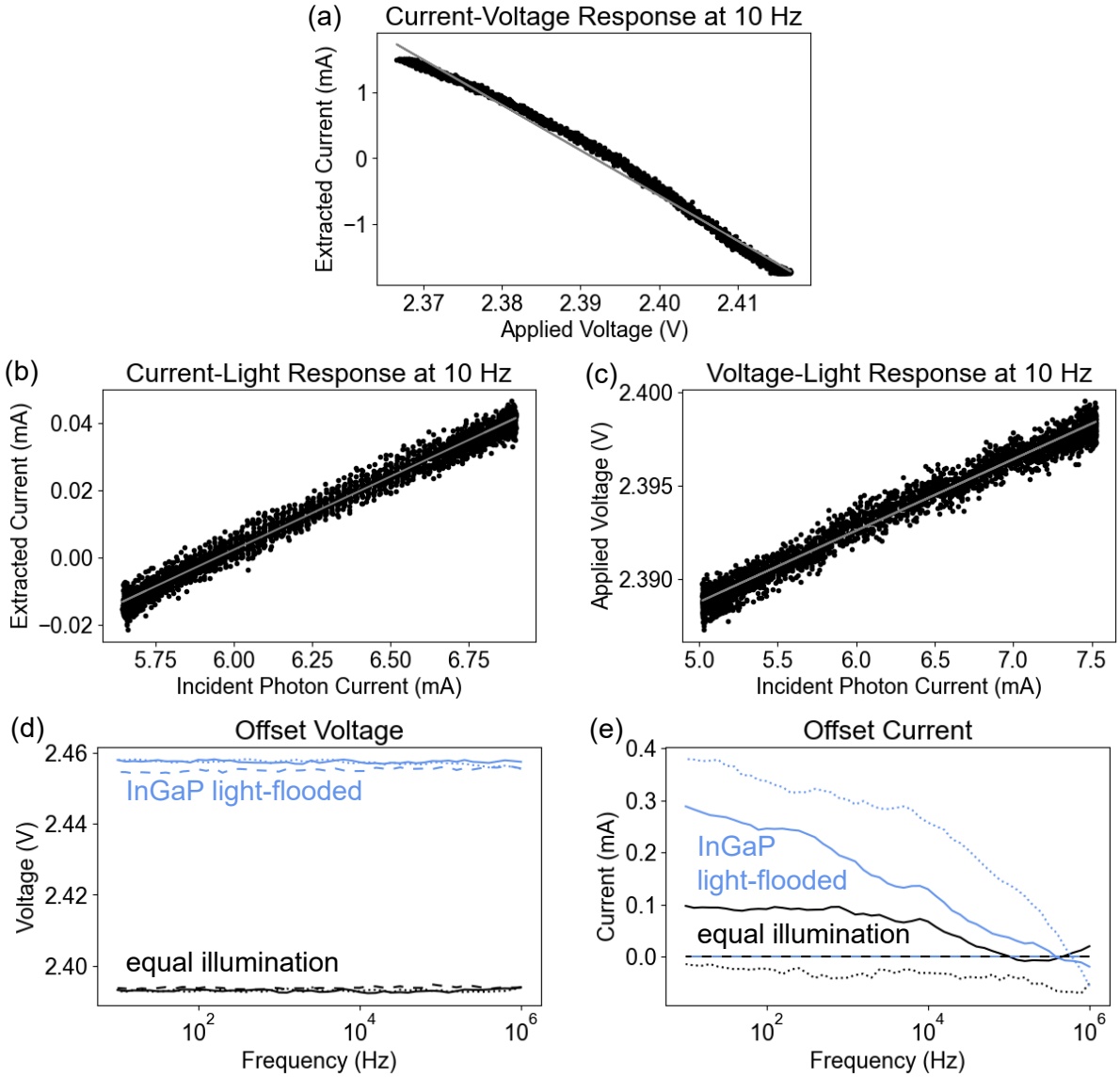

Figure 33. Raw data of (a) the current-voltage response, (b) current-light response, and (c) voltage-light response at 10 Hz under 0.1 suns-equivalent illumination, as well as (d) the offset voltage and (e) offset current over the full frequency range for different illumination conditions of the III-V tandem solar cell with light-modulations perturbing the bottom subcell. Under equal illumination, both subcells are illuminated with 0.1 suns with a modulation in the far-red LED, whereas under light-flooding, a subcell has the same amount of extracted photogenerated charge carriers as under 1 sun illumination. For subfigures (d) and (e), the full, dotted, and dashed lines correspond to the data from the impedance, intensity-modulated photocurrent, and intensity-modulated photovoltage spectroscopy measurements, respectively.